

1 **Blowing snow contributions to the Arctic snow-on-sea ice**  
2 **budget using ICESat-2 observations**

3  
4 Joseph Robinson<sup>1</sup>, Lyatt Jaeglé<sup>1</sup>, Stephen P. Palm<sup>2,3</sup>, Glen E. Liston<sup>4</sup>

5  
6 <sup>1</sup> Department of Atmospheric and Climate Science, University of Washington, Seattle, WA, USA

7 <sup>2</sup> Science Systems and Applications, Lanham, MD, USA

8 <sup>3</sup> NASA Goddard Space Flight Center, Greenbelt, MD, USA

9 <sup>4</sup> Cooperative Institute for Research in the Atmosphere (CIRA), Colorado State University, Fort Collins, CO, USA

10  
11 *Correspondence to:* Joseph Robinson ([jrobin15@uw.edu](mailto:jrobin15@uw.edu))

## 47 **Abstract**

48  
49 Blowing snow modulates the evolution of snow over Arctic sea ice through redistribution and  
50 sublimation. Here, we present the first multi-year pan-Arctic observational estimates of blowing  
51 snow occurrence, properties, and associated fluxes based on NASA Ice, Cloud and land  
52 Elevation Satellite 2 (ICESat-2) satellite observations for five cold seasons (November through  
53 April 2018-2023). On average, ICESat-2 detects blowing snow 19% of the time over sea ice,  
54 with localized frequencies reaching up to 35% in the Central Arctic, where blowing snow heights  
55 (optical depths) reach 150 m (0.20). We find that blowing snow occurrence shows strong  
56 interannual variability related to large-scale climate variability, particularly the Arctic Oscillation  
57 (AO). During positive AO phases, blowing snow occurrence increases substantially, with up to a  
58 two-fold increase in the Central Arctic. Blowing snow occurrence, height, and optical depth all  
59 exhibit a strong dependence on wind speed, increasing by more than five-fold between 4 and 15  
60  $\text{m s}^{-1}$ . ICESat-2 blowing snow sublimation estimates average 1.63 cm snow-water-equivalent  
61 (SWE) per cold season, thus removing 14% of pan-Arctic snowfall. In the Central Arctic, the  
62 offset is 18-24%. These values are consistent with simulations from the high-resolution  
63 SnowModel-LG (1.66 cm SWE) and a simpler, threshold-based model (2.07 cm SWE).  
64 Interannual variability in snowfall and sublimation can be 1-2 cm SWE, though not always in  
65 phase, resulting in snowfall removals that range from 9% to 20%. Critically, these findings  
66 provide satellite-based constraints on blowing snow processes over sea ice and underscore the  
67 importance of blowing snow sublimation in the Arctic snow budget.

## 68 69 **1 Introduction**

70  
71 Snow cover on sea ice is a fundamental component of the Arctic climate system, influencing  
72 surface albedo, insulating the ocean from the atmosphere, and modulating the exchange of heat  
73 and moisture across the ocean-ice-atmosphere interface (Merkouriadi, Cheng, et al., 2017;  
74 Merkouriadi, Gallet, et al., 2017; Sturm et al., 2002; Webster et al., 2018). Its presence impacts  
75 not only the local energy balance but also broader climate feedbacks that affect both high- and  
76 mid-latitudes. As the Arctic undergoes rapid environmental change, including thinning sea ice  
77 (Kwok & Untersteiner, 2011; Stroeve & Notz, 2018), shifting precipitation patterns (Bintanja,  
78 2018; Bintanja & Andry, 2017; McCrystall et al., 2021), and increasing temperatures (Rantanen  
79 et al., 2022), the need to accurately characterize the spatial and temporal variability of snow on  
80 sea ice has become increasingly urgent. Understanding how the snowpack and its properties  
81 evolve across a range of spatial and temporal scales and in response to dynamic atmospheric  
82 processes is essential for improving predictions of sea ice behavior, refining climate model  
83 simulations, and assessing implications for Arctic ecosystems, human activities, and global  
84 climate.

85  
86 While the snowpack on sea ice generally follows a seasonal cycle of winter accumulation and  
87 summer melt, shorter-term processes can alter characteristics and accumulation rates. One such  
88 process is blowing snow, which occurs when strong winds lift snow away from the surface.  
89 Numerous studies spanning several decades have underscored the role of blowing snow in  
90 modulating sea and land ice mass balance (Déry & Yau, 2002; Gallée et al., 2001; Palm et al.,  
91 2017), altering radiative properties in polar regions (Lesins et al., 2009; Y. Yang et al., 2014),  
92 impacting chemical processes in the polar troposphere (Frey et al., 2020; Gong et al., 2023; J.

93 Huang et al., 2020; J. Huang & Jaeglé, 2017; Krnavek et al., 2012; X. Yang et al., 2008), and  
94 complicating the interpretation of physical and chemical ice core records (King et al., 2004;  
95 Rhodes et al., 2017). Yet, capturing the full spatial and temporal variability of blowing snow  
96 remains challenging due to the limited availability of sustained, regionally comprehensive  
97 observations (Déry & Yau, 2001; Mann et al., 2000; Nishimura & Nemoto, 2005).

98  
99 When lifted into the air, blowing snow particles are exposed to conditions that can promote their  
100 sublimation, making blowing snow sublimation a significant pathway for both snow removal and  
101 a source of atmospheric moisture. While sublimation can occur directly at the snow surface, it is  
102 far more efficient when particles are suspended aloft, where their full surface area interacts with  
103 the ambient air (Liston & Sturm, 2004; Schmidt, 1982). In addition, fragmentation within the  
104 saltation layer may generate smaller particles that are readily suspended, increasing mass flux  
105 and further enhancing sublimation rates (N. Huang et al., 2025). Model-based assessments  
106 suggest a substantial role for blowing snow sublimation in the Arctic hydrological cycle: J. Yang  
107 et al. (2010) estimated that over 27% of winter snowfall poleward of 70°N may be lost to  
108 blowing snow sublimation. However, other modeling studies (e.g., Chung et al., 2011; Déry &  
109 Yau, 2002) have reported much lower estimates (6-7%), underscoring the considerable  
110 uncertainty that still surrounds blowing snow related processes. Narrowing these uncertainties  
111 and understanding the implications of sublimation-driven snow loss over sea ice remains a  
112 pressing scientific challenge.

113  
114 The time evolution of snow-water-equivalent (SWE) depth can be described by the mass balance  
115 equation:

$$117 \quad \frac{dSWE}{dt} = \frac{1}{\rho_w} [P - (M + Q_{ss} + Q_{bs}) + Q_t] \quad (1)$$

118  
119 where  $\rho_w$  is the density of water, and the terms represent inputs from precipitation ( $P$ ;  $\text{kg m}^{-2} \text{s}^{-1}$ )  
120 and losses via melt ( $M$ ,  $\text{kg m}^{-2} \text{s}^{-1}$ ) and sublimation ( $\text{kg m}^{-2} \text{s}^{-1}$ ), either from a static, non-blowing  
121 snow surface ( $Q_{ss}$ ) or via blowing snow ( $Q_{bs}$ ). Erosion and deposition by blowing snow transport  
122 ( $Q_t$ ,  $\text{kg m}^{-2} \text{s}^{-1}$ ) can also play a role in shaping the local snowpack. While Eq. 1 represents key  
123 drivers of snowpack evolution, other processes, such as ice dynamics (e.g., creation and  
124 destruction of parcels through ice motion, divergence, and convergence), may also play  
125 important roles.

126  
127 Efforts to quantify the influence of blowing snow on SWE often rely on empirical  
128 parameterizations of snow transport and sublimation derived from sparse observations. These  
129 approaches typically use meteorological inputs such as windspeed, air temperature, and snow age  
130 to estimate thresholds for blowing snow initiation and subsequent sublimation (e.g., Gallée et al.,  
131 2001, 2013; Lenaerts et al., 2010, 2012). In the Northern Hemisphere, model development has  
132 primarily focused on continental snowpacks (Déry & Yau, 2001, 2002; Pomeroy et al., 1997; J.  
133 Yang & Yau, 2007), where snow redistribution is critical to understand human relevant  
134 hydrology and impacts to infrastructure. Although several studies have extended these  
135 approaches to sea ice environments (Chung et al., 2011; Déry & Tremblay, 2004; Lecomte et al.,  
136 2015; Liston et al., 2018, 2020; J. Yang et al., 2010), there remains a lack of direct, observation-  
137 based constraints on pan-Arctic blowing snow processes over sea ice.

139 Spaceborne lidars offer a powerful means to address observational gaps and assess the  
140 occurrence and impacts of blowing snow across large spatial and temporal domains. Palm et al.  
141 (2011, 2017, 2018) developed a detection algorithm for the Cloud-Aerosol Lidar with  
142 Orthogonal Polarization (CALIOP) aboard NASA’s CALIPSO satellite (Winker et al., 2009),  
143 demonstrating that lidar backscatter measurements can be used to quantify key blowing snow  
144 characteristics over Antarctica, including frequency of occurrence, height, optical depth, and  
145 associated transport and sublimation fluxes. Building on this approach, a similar algorithm was  
146 later adapted for the NASA Ice, Cloud, and land Elevation Satellite-2 (ICESat-2; Markus et al.,  
147 2017) by Palm et al. (2021) and Herzfeld et al. (2021). Both algorithms were tailored to detect  
148 blowing snow over the Antarctic continent. More recently, Robinson et al. (2025) optimized the  
149 ICESat-2 blowing snow detection algorithm for application over Arctic sea ice, where more  
150 frequent low-level cloud cover (Shupe et al., 2011; Zhang et al., 2019) increases the likelihood of  
151 both false positives (i.e., clouds misidentified as blowing snow) and false negatives (i.e., blowing  
152 snow misclassified as clear air) in lidar retrievals. Robinson et al. (2025) demonstrated that  
153 retrieval errors caused by cloud interference can be effectively corrected, enabling the  
154 development of a space-based blowing snow detection product specifically adapted for Arctic  
155 sea ice.

156  
157 In this study, our goal is to examine blowing snow occurrence and properties inferred from  
158 ICESat-2 over Arctic sea ice across five cold seasons (defined as November through April)  
159 between 2018 to 2023. We use ICESat-2 observations to infer blowing snow sublimation and its  
160 role in the snow-on-sea ice budget. We compare the ICESat-2 observations to blowing snow  
161 simulations from two models of varying complexity: a parameterization based on the PIEKTUK  
162 blowing snow model (DY2001; Déry & Yau, 1999, 2001; J. Yang & Yau, 2007) and the state-of-  
163 the-art Lagrangian snow-evolution model SnowModel-LG (Liston et al., 2020).

164  
165 In Section 2 we provide details on the ICESat-2 blowing snow retrievals and inferred blowing  
166 snow properties, SnowModel-LG predictions, and the DY2001 blowing snow sublimation  
167 formulation. In Section 3 we present the ICESat-2 multi-year blowing snow occurrence  
168 frequency and properties, examining key drivers of their spatiotemporal distribution. The role of  
169 blowing snow in the snow-on-sea-ice budget is examined in Section 4 and conclusions are  
170 presented in Section 5.

171

## 172 **2 Datasets and Methods**

### 173 **2.1 Satellite blowing snow retrievals from ICESat-2**

174

175 ICESat-2 was launched in 2018 in a precessing orbit with an altitude of  $\sim 500$  km and inclination  
176 of  $92^\circ$ , which allows for measurements up to  $88^\circ$  N latitude with a 91-day orbital repeat cycle  
177 (Markus et al., 2017). ICESat-2 carries the Advanced Topographic Laser Altimeter System  
178 (ATLAS), which is a single wavelength (532 nm), high repetition rate (10 kHz) lidar system with  
179 photon counting detectors (Markus et al., 2017; Neumann et al., 2019). Each ATLAS laser pulse  
180 is split into 3 simultaneous beam pairs (one strong and one weak beam per pair) by a diffractive  
181 optical element. The 3 beam pairs are separated by about 3 km across track. Atmospheric  
182 backscatter is obtained by ATLAS using only the three strong beams, spanning from the surface  
183 to an altitude of 14 km, with an along-track resolution of approximately 280 m and a vertical  
184 resolution of 30 m. Each 280 m ICESat-2 atmospheric profile represents the aggregate of 400

185 individual ATLAS laser shots (Palm et al., 2021). In this study we use ICESat-2 strong beam 1  
186 observations from version 6 of the ATLAS/ICESat-2 Level 3A (ATL09) calibrated backscatter  
187 profile product (Palm et al., 2023).

188  
189 The algorithm used to detect blowing snow in ATLAS backscatter profiles is adapted from the  
190 CALIOP approach (Palm et al., 2011) and further detailed in Palm et al. (2021; 2022). When a  
191 surface return is identified and the 10 m wind speed from NASA’s GEOS-5 FP-IT analysis  
192 exceeds  $4 \text{ m s}^{-1}$ , the algorithm compares the near-surface atmospheric backscatter to the expected  
193 molecular (Rayleigh) signal. If the observed signal exceeds a fixed multiple of the molecular  
194 scattering, the algorithm steps upward through each vertical bin until the backscatter drops below  
195 an adaptive threshold (typically  $\sim 2 \times 10^{-5} \text{ m}^{-1} \text{ sr}^{-1}$ ). To be flagged as blowing snow, the detected  
196 feature must touch the ground and be shallower than 500 m. Retrievals deeper than 500m are  
197 classified as diamond dust, which can stretch for a kilometer or more vertically and frequently  
198 reaches the ground (Intrieri & Shupe, 2004). Further, we use the version of the blowing snow  
199 algorithm described in Robinson et al. (2025) which includes modifications to help alleviate  
200 several challenges unique to the Arctic. These modifications serve to 1) minimize the  
201 misidentification of low clouds as blowing snow and 2) correct for the attenuation due to  
202 transmissive clouds.

203  
204 Once blowing snow is retrieved, its properties (geometric and optical depths) are logged. Optical  
205 depth (OD) is estimated as the sum of the backscatter within the blowing snow retrieval  
206 multiplied by the product of the bin depth (30 m) and the extinction to backscatter (lidar) ratio. A  
207 lidar ratio of 25 sr is used, which is a typical value for ice crystals in cirrus clouds (Chen et al.,  
208 2002; Josset et al., 2012). To infer blowing snow particle number density, transport flux, and  
209 sublimation flux from the observed ICESat-2 backscatter we follow the same approach as  
210 described in Palm et al. (2017) and Robinson et al. (2025), which relies on meteorological fields  
211 (10 m wind speed, 2 m temperature, and 2 m relative humidity over ice) from the NASA GEOS-  
212 5 FP-IT analysis (run at  $0.5^\circ$  latitude  $\times$   $0.625^\circ$  longitude; Lucchesi et al., 2015) as well as  
213 assumptions about blowing snow particle size. As in Robinson et al. (2025) we use the  
214 formulation  $r(z) = 5.05 \times 10^{-5} z^{-0.085}$  to estimate the particle radius ( $r$ , meters) as a function of  
215 altitude ( $z$ , meters). This fit was constrained by observations of blowing snow particle sizes  
216 during the 2019-2020 Multidisciplinary drifting Observatory for the Study of Arctic Climate  
217 (MOSAiC) campaign.

218  
219 To improve signal-to-noise in sunlit conditions, we apply along-track averaging to the ICESat-2  
220 observations when the solar elevation angle exceeds  $-7^\circ$ , a threshold beyond which background  
221 solar photons begin to significantly degrade sensitivity. Under these conditions, which affect late  
222 February through April (Fig. S1), increased solar background can reduce the detectability of low-  
223 backscatter features such as blowing snow. To mitigate this, we average the native 25 Hz (280  
224 m) profiles to 1 Hz ( $\sim 7$  km) resolution, effectively reducing solar background noise and  
225 enhancing the reliability of blowing snow retrievals. While this approach lowers spatial  
226 resolution, it reduces false positive detections and provides a more robust estimate of blowing  
227 snow properties under marginal lighting conditions without introducing significant biases in  
228 seasonal statistics.

229  
230 **2.2 Blowing snow model simulations from SnowModel-LG**

231  
232 SnowModel-LG is a physics-based snow-on-sea ice model forced by atmospheric inputs of air  
233 temperature, RH, winds, and precipitation from the NASA Modern-Era Retrospective analysis  
234 for Research and Applications, version 2 (MERRA-2; Gelaro et al., 2017) as well as sea ice  
235 inputs of concentration and parcel motion (Tschudi et al., 2019, 2020). At each 3-hour timestep,  
236 SnowModel-LG performs mass-budget calculations (e.g., Eq. 1) where SWE depth evolution is  
237 accounted for by snow gains, losses, and sea ice dynamics (Liston et al., 2020).

238  
239 The MicroMet module (Liston & Elder, 2006) is used to time average (1-hourly to 3-hourly) and  
240 distribute the MERRA-2 fields ( $0.5^\circ$  latitude  $\times$   $0.625^\circ$  longitude) to the sea ice parcels. As part of  
241 this procedure, the MERRA-2 water equivalent precipitation is bias corrected (as described in  
242 section 2.5 and Table 1 of Liston et al., (2020)) and partitioned into snowfall and rainfall based  
243 on environmental conditions (Dai, 2008).

244  
245 Blowing snow in SnowModel-LG is accounted for by SnowTran-3D (Liston et al., 2007, 2018;  
246 Liston & Sturm, 1998). The snow threshold friction velocity,  $u_{*t}$ , is calculated as a function of  
247 snow density,  $\rho_s$ , which is related to snow strength and hardness. Snow density evolution  
248 includes the history of temperature, precipitation, and wind-transport. When the friction velocity  
249 exceeds the threshold value, snow begins to be lifted off the surface, first into the saltation layer  
250 (several cm thick) and then into the turbulent suspension layer (several m thick). The vertical  
251 mass concentration in the blowing snow profile is estimated following Liston & Sturm (1998)  
252 and is combined with the environmental conditions to calculate transport and sublimation fluxes.  
253 Mass transport is related to the windspeed and vertical mass concentration. SnowModel-LG's  
254 blowing snow sublimation is calculated as a function of several factors, including the vertical  
255 mass concentration, temperature-dependent humidity gradients between the snow particles and  
256 the atmosphere, conductive and advective energy- and moisture-transfer mechanisms, particle  
257 size, and solar radiation. The SnowModel-LG blowing snow transport and sublimation fluxes  
258 represent column integrated values in units of  $\text{kg m}^{-1} \text{s}^{-1}$  and  $\text{cm SWE d}^{-1}$ , respectively.  
259 SnowModel-LG variables are output as 3-hourly values on an EASE grid with a resolution of 25  
260 km.

### 261 262 **2.3 Blowing snow sublimation estimates from DY2001**

263  
264 We also include estimates of the bulk blowing snow sublimation rate ( $Q_{bs}$  in Eq. 1) using the  
265 approach described by Déry & Yau (1999, 2001) and subsequently J. Yang & Yau (2007).  
266 Throughout the analysis we refer to this approach as DY2001. We chose to include it because it  
267 is computationally efficient and has been widely applied in studies of blowing snow aerosol  
268 production over sea ice (e.g., Gong et al., 2023; Frey et al., 2020; J. Huang et al., 2020; J. Huang  
269 & Jaeglé, 2017; X. Yang et al., 2008, 2019). Sublimation depends on several factors including  
270 surface windspeed, temperature, and humidity deficit.

271  
272 Following X. Yang et al. (2008), sublimation is scaled by snow age  $A'$  which accounts for the  
273 reduced ease of wind lofting as snow ages. For a full description of the sublimation calculation  
274 used here, we refer the reader to section 2.1.1 of X. Yang et al. (2008). In our calculations, we  
275 adopt a representative mean snow age of 3 days over Arctic sea ice (J. Huang & Jaeglé, 2017).

276

277 A key factor controlling blowing snow occurrence in DY2001 is the threshold windspeed, which  
278 follows Li & Pomeroy (1997a). The threshold windspeed ( $U_t = 6.975 + 0.0033[T_{2m} + 27.27]^2$ ) is  
279 estimated from the 2 m surface air temperature ( $T_{2m}$ ) and has a minimum value of  $\sim 7 \text{ m s}^{-1}$  at an  
280 air temperature of  $-27^\circ\text{C}$ . At both higher and lower temperatures, the threshold wind speed will  
281 be larger (maximizing at  $\sim 10 \text{ m s}^{-1}$  for temperatures near  $0^\circ\text{C}$ ). We estimate the DY2001  
282 threshold windspeed and blowing snow sublimation using the same meteorology (10 m  
283 windspeed, 2 m temperature, and 2 m  $\text{RH}_{\text{ice}}$ ) used to derive the ICESat-2 sublimation.

284

## 285 **2.4 ICESat-2 and model gridding procedure**

286

287 We aggregate the ICESat-2 observations to a National Snow and Ice Data Center (NSIDC)  
288 Equal-Area Scalable Earth (EASE) grid (Brodzick & Knowles, 2002) with a horizontal resolution  
289 of 100 km. This resolution balances spatial detail with observational coverage, ensuring  
290 sufficient ICESat-2 sampling within each grid cell while minimizing noise that would arise at  
291 finer resolutions due to the narrow swath of the lidar. Temporal resolution is determined by the  
292 duration of the binning period, allowing flexibility to examine daily, seasonal, or multi-year  
293 patterns.

294

295 Within each 100 km grid cell, the ICESat-2 blowing snow occurrence for a specified time  
296 window is computed as the number of profiles with a blowing snow detection divided by the  
297 total number of valid profiles. A valid profile is defined as one where the surface return is clearly  
298 detected, which excludes profiles with optically thick cloud cover (optical depth  $> 3$ ), where  
299 surface detection is unreliable or is not achieved. For blowing snow properties such as geometric  
300 and optical depths, only blowing snow retrievals are gridded.

301

302 For comparison with model estimates, we extract values from the SnowModel-LG fields (25 km  
303 resolution) by sampling the nearest-neighbor grid point to each valid ICESat-2 profile location.  
304 These sampled values are then binned to the same 100 km EASE grid alongside the ICESat-2  
305 data. We apply the same procedure to the DY2001 estimates: values are first computed at the  
306 location of each valid ICESat-2 profile, and the resulting fields are aggregated onto the 100 km  
307 grid for direct comparison with both ICESat-2 observations and SnowModel-LG outputs.

308

## 309 **2.5 December 2022 example of observed and predicted blowing snow**

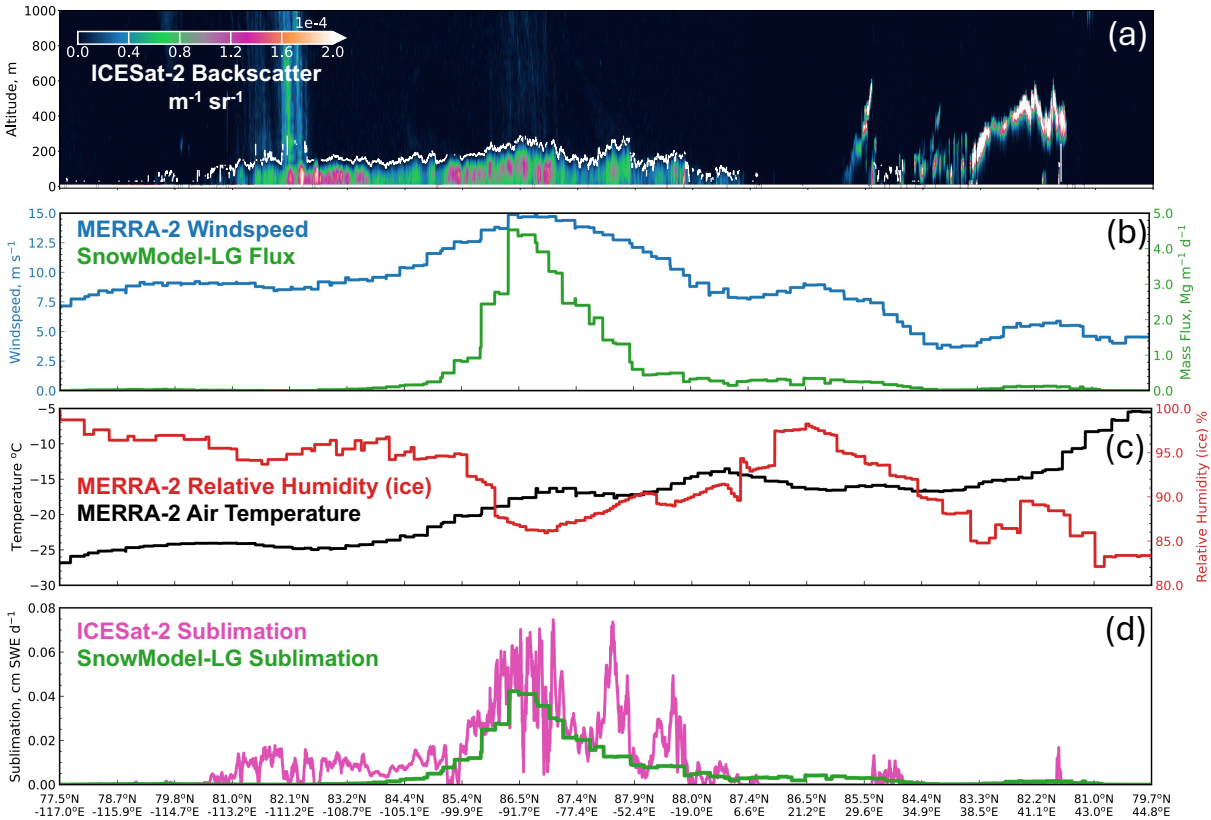
310

311 Figure 1 highlights a blowing snow storm which occurred over the Central Arctic on 10  
312 December 2022. During an orbit which transited from the Canadian Arctic Archipelago towards  
313 Svalbard, ICESat-2 retrieved blowing snow for roughly 1,200 km along track, with depths up to  
314 250 m and observed attenuated backscatter exceeding  $1.50 \times 10^{-4} \text{ m}^{-1} \text{ sr}^{-1}$  (Fig. 1a). In this region,  
315 MERRA-2 windspeeds ranged from  $7.5$  to  $15 \text{ m s}^{-1}$  (blue line, Fig. 1b) and SnowModel-LG  
316 predicted intense blowing snow, with mass fluxes peaking at  $4 \text{ Mg m}^{-1} \text{ d}^{-1}$  (green line, Fig. 1b).  
317 The strongest ICESat-2 observed and SnowModel-LG predicted blowing snow occurred  
318 coincident with the strongest winds (middle of Fig. 1a,b). While ICESat-2 did retrieve blowing  
319 snow to the west of this maximum (left side, Fig. 1a) coincident with windspeeds  $> 8 \text{ m s}^{-1}$ ,  
320 SnowModel-LG predicted only minimal blowing snow mass transport.

321

322 At the location of intense blowing snow, MERRA-2 air temperatures ranged from  $-25^{\circ}\text{C}$  to  $-15^{\circ}\text{C}$   
 323 (black line, Fig. 1c) and the air was subsaturated with respect to ice (85-95%; red line, Fig. 1c).  
 324 This combination of meteorological factors resulted in substantial blowing snow sublimation  
 325 inferred from ICESat-2 and predicted by SnowModel-LG (Fig. 1d). ICESat-2 sublimation  
 326 maximized at  $0.07\text{ cm SWE d}^{-1}$  coincident with the strongest winds and driest conditions  
 327 (magenta line, Fig. 1d). In the same region SnowModel-LG sublimation reached  $0.05\text{ cm SWE}$   
 328  $\text{d}^{-1}$  (green line, Fig. 1d).  
 329

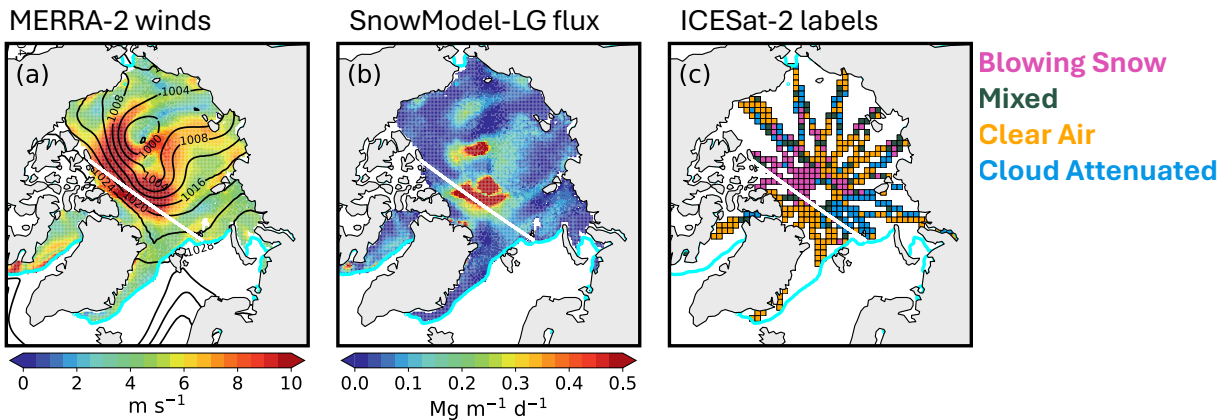
Blowing Snow Case: 10 December 2022



330  
 331  
 332 **Figure 1.** Case study of a blowing snow event in the Central Arctic on 10 December 2022. **(a)** ICESat-2 attenuated  
 333 backscatter (shading, units  $\text{m}^{-1}\text{ sr}^{-1}$ ) along an orbit from the Canadian Arctic Archipelago towards north of Svalbard.  
 334 The white line indicates the top of the blowing snow layer. **(b)** MERRA-2 windspeed (blue line, units  $\text{m s}^{-1}$ ) and  
 335 SnowModel-LG blowing snow mass transport (green line, units  $\text{Mg m}^{-1}\text{ d}^{-1}$ ) along the ICESat-2 orbit shown in panel  
 336 a. **(c)** Near-surface MERRA-2 air temperature (black line, units  $^{\circ}\text{C}$ ) and relative humidity over ice (red line, units %)  
 337 along the ICESat-2 orbit shown in panel a. **(d)** Blowing snow sublimation (units  $\text{cm SWE d}^{-1}$ ) inferred from ICESat-  
 338 2 (magenta line) and predicted by SnowModel-LG (green line) along the ICESat-2 orbit shown in panel a. To reduce  
 339 noise, the ICESat-2 sublimation has been averaged with a moving 8 km along-track window.  
 340

341 Winds in excess of  $8\text{ m s}^{-1}$  covered much of the Central Arctic and coincided with tight sea-level  
 342 pressure (SLP) gradients stretching from the Beaufort to Lincoln Sea (Fig. 2a). SnowModel-LG  
 343 predicted blowing snow mass transport  $> 0.20\text{ Mg m}^{-1}\text{ d}^{-1}$  over an area of  $750,000\text{ km}^2$  (Fig. 2b),  
 344 which is slightly larger in size than the state of Texas. Given a total Central Arctic area of  
 345 roughly  $3.2\text{ million km}^2$ , this storm impacted about a quarter of the basin.  
 346

347 To examine the spatial distribution of ICESat-2 profiles, we first gridded the ICESat-2 orbits to  
 348 the 100 km grid (Section 2.4) and then assigned each grid cell to one of four categories: blowing  
 349 snow, mixed, clear air, or cloud attenuated. If more than 70% of all profiles were attenuated due  
 350 to clouds, the grid cell was labeled as cloud attenuated. We assigned the other three categories  
 351 based on the occurrence of blowing snow: blowing snow if more than 50% of profiles were  
 352 blowing snow, mixed if 15-50% of profiles were blowing snow, and clear air if less than 15% of  
 353 profiles were blowing snow. ICESat-2 grid cells in the western Central Arctic were consistently  
 354 classified as blowing snow (magenta colors, Fig. 2c), coinciding with the strongest winds and the  
 355 highest SnowModel-LG predicted transport. The total area of ICESat-2 grid cells labeled as  
 356 blowing snow was 740,000 km<sup>2</sup>, closely matching the SnowModel-LG predictions and  
 357 confirming that the blowing snow was synoptic in scale, covering much of the Central Arctic.  
 358



359 **Figure 2.** Arctic-wide spatial structure of the 10 December 2022 blowing snow event. (a) Spatial distribution of  
 360 MERRA-2 windspeed (shading, units m s<sup>-1</sup>) with sea-level pressure contours (black, 4 hPa intervals). (b) Spatial  
 361 distribution of SnowModel-LG blowing snow mass transport (shading, units Mg m<sup>-1</sup> d<sup>-1</sup>). (c) ICESat-2  
 362 classifications at 100 km resolution: blowing snow (magenta), mixed (green), clear air (orange), or cloud attenuated  
 363 (blue) as described in Section 2.5. In panels a-c, the cyan line marks the 15% sea ice contour, while the white line  
 364 shows the track of ICESat-2 from Figure 1a.  
 365

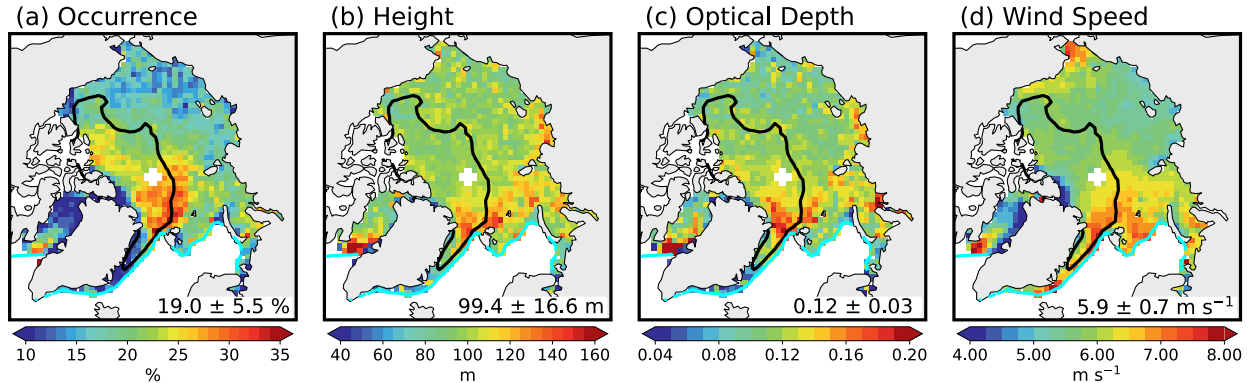
### 366 **3 Blowing snow occurrence frequency and properties from ICESat-2**

#### 367 **3.1 Spatiotemporal variability and drivers of blowing snow occurrence**

368  
 369 Figure 3 shows the mean multi-year blowing snow occurrence and properties derived from the  
 370 ICESat-2 observations for November through April 2018-2023. To generate the average maps,  
 371 we grid each cold season independently (following Section 2.4) and then average the five cold  
 372 seasons together. We found a significant fraction of the central Arctic experiences blowing snow  
 373 frequencies > 25%, with maxima of near 35% in the Fram Strait region (Fig. 3a). This is  
 374 consistent with several previous studies which showed these regions have consistent influence (>  
 375 15% of the time) from storms entering the Arctic (e.g., Clancy et al., 2022; Valkonen et al.,  
 376 2021). This is also evident in the spatial distribution of MERRA-2 windspeeds (Fig. 3d), where  
 377 the region of high blowing snow occurrence frequency is collocated with average windspeeds >  
 378 6.5 m s<sup>-1</sup>.  
 379

380  
 381 The delineation between first- and multi-year sea ice (Tschudi et al., 2020) lies north of the Fram  
 382 Strait and visibly bifurcates the region of elevated ICESat-2 derived blowing snow occurrence  
 383 (Fig. 3a). In a recent study focused on Svalbard, Li et al. (2025) found that observed increases in

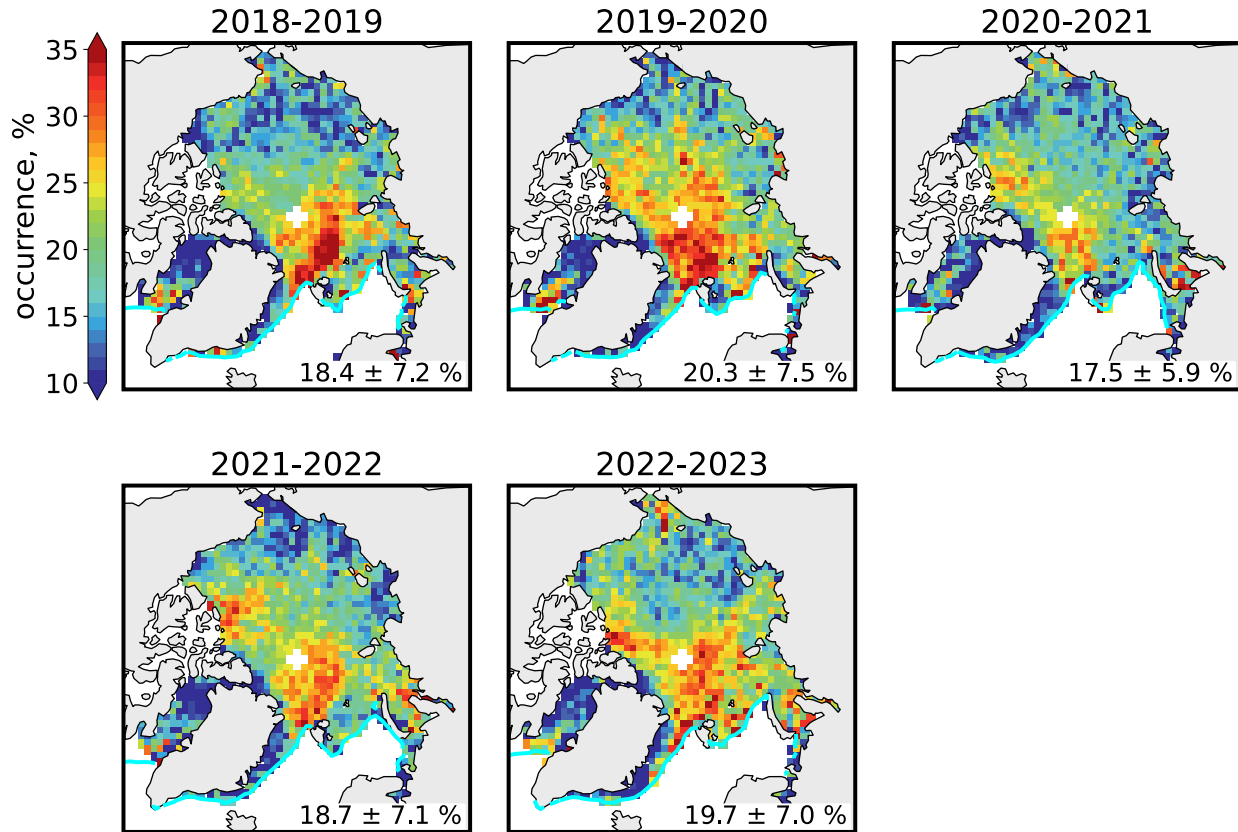
384 tropospheric bromine were correlated with air mass contact over sea ice under strong winds, and  
 385 that boundary layer air masses reaching Svalbard spent more time over multi-year sea ice  
 386 compared to first-year sea ice. The spatial pattern shown in Fig. 3a is consistent with these  
 387 findings, where storms entering the Arctic drive strong north-northwesterly winds that  
 388 preferentially advect air masses across the multi-year ice zone towards Svalbard.  
 389



390  
 391 **Figure 3.** Mean ICESat-2 blowing snow properties during the cold season (November-April, 2018-2023): (a)  
 392 occurrence frequency, (b) blowing snow geometrical depth, (c) optical depth, and (d) MERRA-2 10 m wind speed.  
 393 The cyan line marks the 15% sea ice contour and the black line delineates regions of first- and multi-year sea ice  
 394 (defined as multi-year ice constituting more than half of the total sea ice concentration). Numbers in the bottom right  
 395 of each panel correspond to the mean and standard deviation for values over sea ice.  
 396

397 The ICESat-2 occurrence frequency does not include shallow (< 30 m thick) blowing snow  
 398 layers, since these cannot be reliably detected at the vertical resolution of the atmospheric  
 399 backscatter profiles. In addition, ICESat-2 cannot sample conditions where optically thick clouds  
 400 prevent the surface from being detected. Regions of the Kara, Barents, and Greenland Seas are  
 401 particularly susceptible to this under sampling, where the ICESat-2 cloud attenuated occurrence  
 402 (% of all profiles where the surface cannot be detected) can exceed 50% across much of the cold  
 403 season (Fig. S2).  
 404

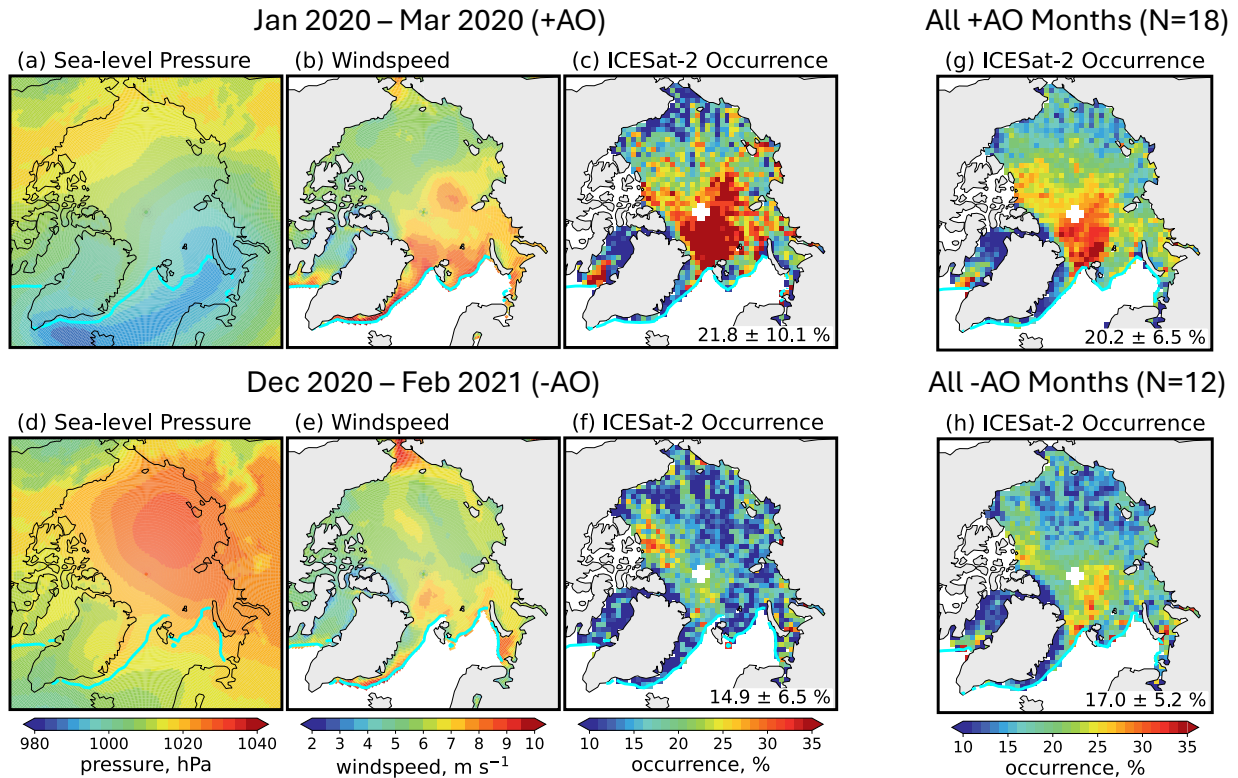
405 The multi-year cold season ICESat-2 retrievals show blowing snow layers averaging ~ 100 m in  
 406 depth, ranging from ~ 50 m up to 160 m (Fig. 3b). Our previous analysis of ICESat-2  
 407 observations near the 2019-2020 MOSAiC campaign demonstrated that low level turbulence  
 408 often mixes blowing snow to the top of the surface inversion (Robinson et al., 2025), suggesting  
 409 that blowing snow layer depth may serve as a useful indicator of Arctic inversion depth. Blowing  
 410 snow optical depths average 0.12 across the Arctic, with maxima near 0.20 in the Fram Strait and  
 411 southern Baffin Bay (Fig. 3c). These regions also experience thicker blowing snow layers on  
 412 average. Figure 3 further shows that regions of deeper, optically thicker blowing snow are co-  
 413 located with areas of high occurrence frequency and stronger winds.  
 414



415  
 416 **Figure 4.** Interannual spatial variability of blowing snow occurrence frequency (units %) from ICESat-2  
 417 observations during the 2018-2023 cold seasons. Each panel shows the average pan-Arctic occurrence and standard  
 418 deviation (lower right). The cyan line marks the 15% sea ice concentration contour.  
 419

420  
 421 Figure 4 shows that the ICESat-2 pan-Arctic blowing snow occurrence frequencies are consistent  
 422 from year-to-year at 18-20%. The spatial pattern of occurrence also remains fairly consistent,  
 423 with the Central Arctic and Fram Strait displaying the highest frequencies and only moderate  
 424 shifts in location. Despite this, the Central Arctic can display substantial year-to-year variability.  
 425 For example, the highest (2019-2020) and lowest (2020-2021) pan-Arctic frequencies were  
 426 observed in consecutive cold seasons.  
 427

428 The contrast between these two cold seasons appears closely aligned with large scale climate and  
 429 atmospheric circulation patterns, particularly the Beaufort High and the Arctic Oscillation (AO).  
 430 In early 2020, a record positive AO phase (+3.5, top row Fig. S3) coincided with a collapse of  
 431 the Beaufort High, enhanced cyclone activity (Ballinger et al., 2021; Rinke et al., 2021), and  
 432 widespread blowing snow. From January to March 2020, MERRA-2 sea-level pressure (SLP)  
 433 and windspeed featured an elongated region of consistently low pressure (< 1,000 hPa) extending  
 434 from Iceland into the ice-covered Kara and Barents Seas (Fig. 5a). Over these regions and the  
 435 Central Arctic, mean windspeeds reached 7-9 m s<sup>-1</sup> (Fig. 5b). During this period, ICESat-2  
 436 observed several intense blowing snow episodes covering more than 25% of sea ice area  
 437 (blowing snow > 1×10<sup>6</sup> km<sup>2</sup>; Fig. S4), with mean pan-Arctic blowing snow frequencies of  
 438 21.8%, reaching up to 50% in the Central Arctic (Fig. 5c).  
 439



440  
441

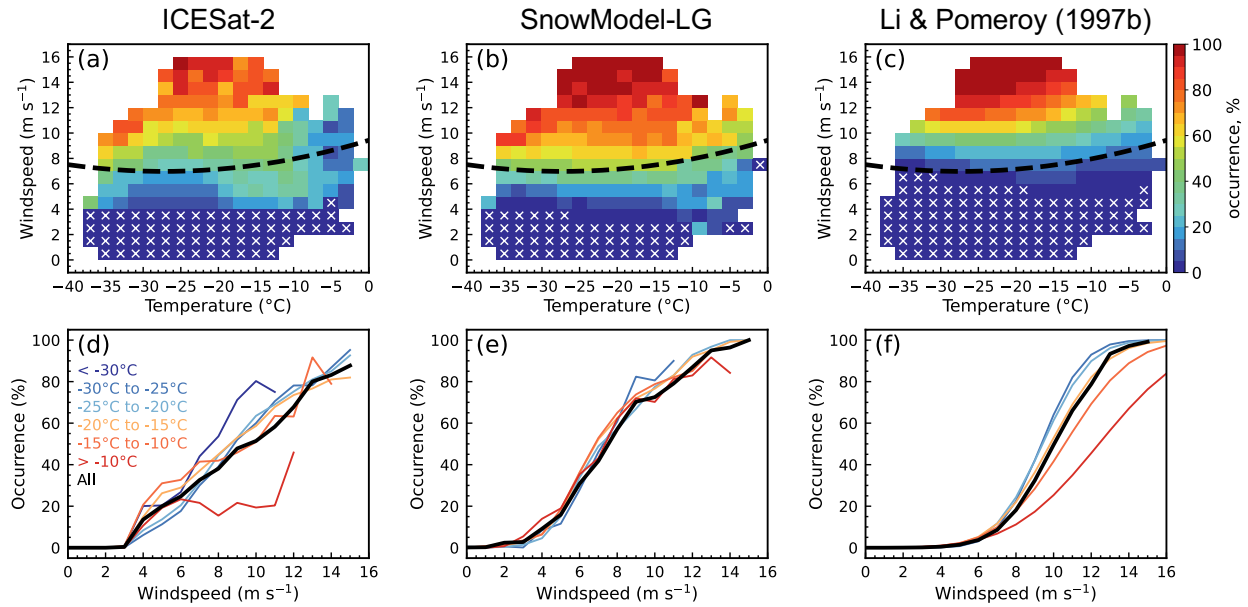
442 **Figure 5.** Comparison of (a,d) MERRA-2 sea-level pressure (hPa), (b,e) MERRA-2 wind speed (m s<sup>-1</sup>), and (c,f)  
443 ICESat-2 observed blowing snow occurrence frequency (%) for January 2020 – March 2020 (a-c) and December  
444 2020 – February 2021 (d-f). (g,h) Composite ICESat-2 blowing snow occurrence frequency for months with (g)  
445 positive and (h) negative Arctic Oscillation phases during the 2018-2023 cold seasons.  
446

447 In contrast, the 2020-2021 season was marked by a strong negative AO (-2.4, top row Fig. S3)  
448 and a persistent Beaufort High (mean MERRA-2 SLP > 1,020 hPa across most of the Arctic  
449 basin, Fig. 5d), conditions known to suppress storm activity (Kenigson & Timmermans, 2021;  
450 Serreze & Barrett, 2011). Consistent with this pattern, MERRA-2 windspeeds were on average ~  
451 2 m s<sup>-1</sup> lower relative to January-March 2020 (Fig. 5e). From December 2020 to February 2021  
452 ICESat-2 detected substantially less blowing snow (47% lower relative to January-March 2020),  
453 with frequencies in the Central Arctic maximizing at only ~ 25% (Fig. 5f). Across all months, we  
454 find a moderately strong correlation between AO phase and ICESat-2 blowing snow occurrence  
455 ( $r = 0.62$ ; Fig. S3c). Composites highlight this relationship: positive AO months (N=18; Fig. 5g)  
456 exhibit 20% more blowing snow than negative AO months (N=12, Fig. 5h), with particularly  
457 large differences (up to a factor of two) in the Fram Strait and Central Arctic.  
458

### 459 3.2 Relationship between windspeed and blowing snow

460

461 In the following section we focus on the Central Arctic region during January-March, the region  
462 most well-sampled by ICESat-2 and months least affected by optically thick clouds (Fig. S2). To  
463 examine relationships between meteorological factors and blowing snow, we use daily 100 km  
464 grid-cell averages. Although this lowers the total number of samples compared to a profile-based  
465 approach, averaging helps to reduce noise.  
466



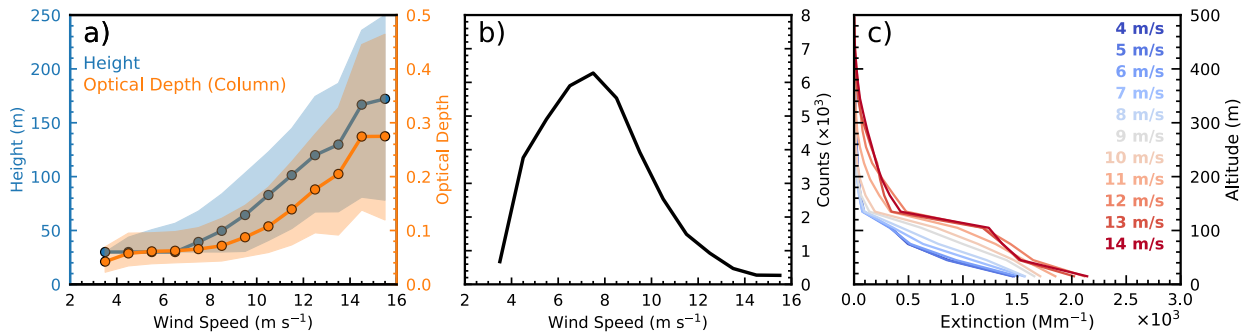
467  
 468  
 469 **Figure 6.** Top row: Dependence of blowing snow occurrence frequency on windspeed and temperature for (a)  
 470 ICESat-2, (b) SnowModel-LG (blowing snow transport fluxes  $> 0.20 \text{ Mg m}^{-1} \text{ d}^{-1}$ ), and (c) Li & Pomeroy (1997b)  
 471 (mean snow age = 72 hours). White stippling represents conditions with no blowing snow; the black dashed line  
 472 shows the DY2001 threshold windspeed. Bottom row: Dependence of blowing snow occurrence frequency on  
 473 windspeed for all temperatures (black), and for different temperature ranges ( $< -30^\circ\text{C}$ ;  $-30^\circ$  to  $-25^\circ\text{C}$ ;  $-25^\circ$  to  $-20^\circ\text{C}$ ;  
 474  $-20^\circ$  to  $-15^\circ\text{C}$ ;  $-15^\circ$  to  $-10^\circ\text{C}$ ;  $> -10^\circ\text{C}$ ) for (d) ICESat-2, (e) SnowModel-LG, and (f) Li & Pomeroy (1997b).  
 475

476 Figure 6 compares the blowing snow occurrence as a function of windspeed and temperature.  
 477 For comparison to ICESat-2 and SnowModel-LG, the blowing snow occurrence from Li &  
 478 Pomeroy (1997b) is also shown (see their Eq. 7). The blowing snow occurrence from Li &  
 479 Pomeroy (1997b) is based on a statistical analysis of observations for 16 stations on the prairies  
 480 of western Canada and is a function of windspeed, temperature, and snow age (assumed in our  
 481 analysis to be 72 hours). It is also in contrast to DY2001, where the threshold windspeed  
 482 essentially acts as an on-off switch for blowing snow. ICESat-2 retrievals indicate a 10-40%  
 483 blowing snow occurrence below the DY2001 threshold of  $\sim 7 \text{ m s}^{-1}$  (black dashed line, Fig. 6a),  
 484 with a much stronger dependence on windspeed than on temperature (Fig. 6a). For example, at 8  
 485  $\text{m s}^{-1}$ , the ICESat-2 occurrence is 50-60% across all temperatures, while at  $-25^\circ\text{C}$  it rises from  
 486 10-15% at  $4 \text{ m s}^{-1}$  to  $> 80\%$  at  $15 \text{ m s}^{-1}$ . SnowModel-LG predictions (defined as blowing snow  
 487 transport  $> 0.20 \text{ Mg m}^{-1} \text{ d}^{-1}$ ) display frequencies  $\sim 10\%$  larger than ICESat-2 on average but  
 488 capture similar features (Fig. 6b). The occurrence of blowing snow predicted from Li & Pomeroy  
 489 (1997b) displays a narrower transition region, increasing sharply from  $< 20\%$  to  $> 60\%$  over the  
 490 8-10  $\text{m s}^{-1}$  range (Fig. 6c).  
 491

492 The one-dimensional distributions (Fig. 6d-f) further emphasize the dominant control of  
 493 windspeed, with all three datasets showing increasing occurrence with stronger winds. ICESat-2  
 494 and SnowModel-LG show a weak temperature dependence, with slightly lower occurrence at  
 495 higher temperatures, especially for stronger winds, consistent with enhanced snow cohesion and  
 496 bonding resistance (Fig. 6d,e). The Li & Pomeroy (1997b) formulation shows a stronger  
 497 temperature sensitivity, ranging from 75% at  $T < -30^\circ\text{C}$  to 20% at  $T > -5^\circ\text{C}$  for a  $10 \text{ m s}^{-1}$   
 498 windspeed (Fig. 6e). The temperature dependence is likely stronger because of our assumption of

499 a fixed snow age of 72 hours. Snow age also influences bonding and cohesion, with older snow  
 500 being more resistant to erosion. Because SnowModel-LG and ICESat-2 sample a range of snow  
 501 ages, their apparent temperature dependence is likely weaker.  
 502

503 ICESat-2 blowing snow properties also show a strong dependence on windspeed (Fig. 7a).  
 504 Median blowing snow layer height increases from 30 m at windspeeds of  $\sim 4 \text{ m s}^{-1}$  to more than  
 505 150 m at windspeeds  $> 14 \text{ m s}^{-1}$ . Optical depth exhibits a similar relationship, rising from 0.02  
 506 to 0.26 over the same windspeed range. The spread in both height and optical depth (shading, Fig.  
 507 7a) also widens with increasing windspeed, which we attribute to increased noise from fewer  
 508 observations in the highest windspeed bins (Fig. 7b).  
 509



510  
 511  
 512 **Figure 7.** Dependence of ICESat-2 blowing snow height and optical depth on windspeed. **(a)** Median (circles with  
 513 line) and interquartile range (shading) of ICESat-2 retrieved blowing snow geometric depth (blue) and optical depth  
 514 (orange) as a function of 10 m windspeed, using  $0.5 \text{ m s}^{-1}$  bins. **(b)** Number of grid cells (in thousands) in each  
 515 windspeed bin from panel a. **(c)** Mean blowing snow extinction profiles (units  $\text{Mm}^{-1}$ ) from ICESat-2 retrievals in  
 516 February 2022 ( $N = 678,914$ ), grouped in  $1 \text{ m s}^{-1}$  wide windspeed bins.  
 517

518 The increase in blowing snow optical depth reflects a combination of increased blowing snow  
 519 height and stronger backscatter signal (Fig. 7c). Across nearly 700,000 ICESat-2 retrievals in  
 520 February 2022, near-surface blowing snow extinction increased by 40% from  $1.5 \times 10^3 \text{ Mm}^{-1}$  at 4  
 521  $\text{m s}^{-1}$  to  $2.1 \times 10^3 \text{ Mm}^{-1}$  at  $14 \text{ m s}^{-1}$ . The enhancement is even larger aloft (a factor of 2-3).  
 522 Together, these results indicate that stronger winds loft more blowing snow higher into the  
 523 atmosphere, consistent with previous studies (Palm et al., 2011, 2018; Robinson et al., 2025).  
 524

#### 525 4 Contribution of blowing snow to the Arctic snow-on-sea ice budget

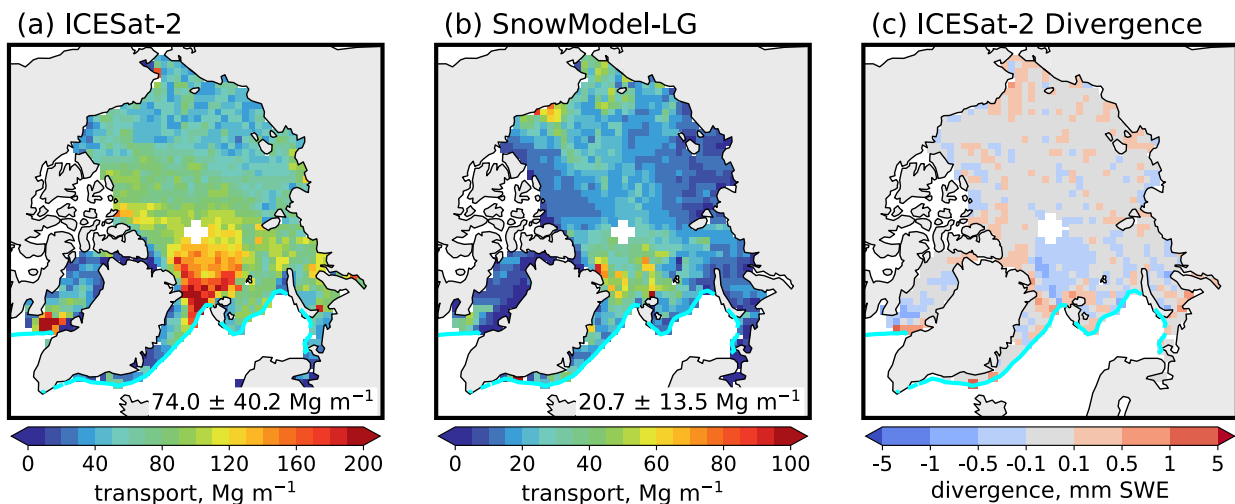
526  
 527 In this section we examine the contribution of blowing snow to the Arctic cold season snow-on-  
 528 sea-ice budget. We focus on column integrated blowing snow mass transport ( $Q_t$  in Eq. 1) and  
 529 sublimation ( $Q_{bs}$  in Eq. 1) fluxes, placing them in the context of one another and comparing them  
 530 to accumulated snowfall. When interpreting the magnitude of the ICESat-2 estimates, we note  
 531 that they depend on assumptions inherent to the backscatter-to-flux conversions (Palm et al.,  
 532 2017; Robinson et al., 2025), including prescribed blowing snow particle sizes and the use of  
 533 modeled meteorological fields to represent near-surface windspeed, temperature, and humidity  
 534 (section 2.1). Blowing snow particle sizes are assumed to decrease exponentially with height,  
 535 while sublimation rates increase with higher temperatures and lower humidities.  
 536  
 537

#### 538 4.1 Blowing snow transport from ICESat-2 and SnowModel-LG

539

540 Figure 8a shows the spatial distribution of blowing snow transport flux inferred from ICESat-2.  
541 The flux is calculated by combining the ICESat-2 derived mass concentrations with the vertical  
542 profile of windspeed, integrated over the depth of the blowing snow layer. The pan-Arctic mean  
543 transport flux observed by ICESat-2 is  $74 \text{ Mg m}^{-1}$ , with maxima  $> 160 \text{ Mg m}^{-1}$  in the Central  
544 Arctic, co-located with regions of frequent and intense blowing snow (Fig. 3). SnowModel-LG  
545 produces a similar spatial distribution but yields transport fluxes that are 2-3 times lower (Fig.  
546 8b). This discrepancy likely arises because SnowModel-LG confines blowing snow to the lowest  
547 several meters of the atmosphere, where winds are weaker. In contrast, ICESat-2 detects blowing  
548 snow layers extending several hundred meters above the surface (Fig. 3b, 7a), where stronger  
549 winds enhance snow transport. To support this interpretation, we examined the pan-Arctic  
550 blowing snow burdens (mass per square meter; Fig. S5) and found that they agree to within  
551 about 20% between ICESat-2 ( $0.17 \text{ g m}^{-2}$ ) and SnowModel-LG ( $0.14 \text{ g m}^{-2}$ ). In the Central  
552 Arctic regions of enhanced transport, both datasets have mean blowing snow burdens of up to  
553  $0.40 \text{ g m}^{-2}$ .

554



555

556

557 **Figure 8.** Mean 2018-2023 cold season blowing snow transport flux ( $\text{Mg m}^{-1}$ ) from (a) ICESat-2 and (b)  
558 SnowModel-LG. Note the color scale for SnowModel-LG is different than for ICESat-2. (c) Divergence of blowing  
559 snow transport inferred from ICESat-2 (mm SWE).

560

561 Although the spatial pattern of transport broadly agrees, our seasonal values are smaller than  
562 those reported by J. Yang et al. (2010). Their simulations for December 2006 – February 2007  
563 suggested transport fluxes up to  $800 \text{ Mg m}^{-1}$  in the Central Arctic and  $> 1,000 \text{ Mg m}^{-1}$  along  
564 Greenland's east coast. These higher values could reflect methodological differences: their  
565 model did not explicitly account for variable snowpack conditions, which could lead to an  
566 overestimate in blowing snow occurrence and transport, and was run at finer spatial (18 km) and  
567 temporal (5 s) resolutions, which could capture small-scale wind gradients and localized  
568 enhancements in snow redistribution. Despite these differences, both our results and those of J.  
569 Yang et al. (2010) indicate that blowing snow transport plays a relatively minor role in the basin-  
570 scale snow budget. For example, the divergence of ICESat-2 transport (Fig. 8c) is limited to a  
571 few tenths of mm SWE, with localized maxima near 1 mm SWE in regions of frequent blowing

572 snow. We further examined the divergence separately for each cold season (Fig. S6), finding that  
573 basin-wide averages remain  $< 10^{-3}$  mm SWE. The divergence exhibits interannual variability  
574 which is largely tied to prevailing meteorological conditions and blowing snow occurrence. For  
575 example, we find substantially greater ICESat-2 inferred divergence during 2019-2020 compared  
576 to 2020-2021, consistent with the AO-phase dependence of blowing snow discussed above (Fig.  
577 5).

578

#### 579 **4.2 Multi-year estimates of blowing snow sublimation**

580

581 Figure 9 shows the mean total annual blowing snow sublimation and snowfall for the 2018-2023  
582 cold seasons. Pan-Arctic blowing snow sublimation totals from ICESat-2 (1.63 cm SWE) are in  
583 close agreement with SnowModel-LG (1.66 cm SWE) and within 30% of DY2001 (2.07 cm  
584 SWE). All three estimates are broadly consistent with previous modeling studies (Chung et al.,  
585 2011; Liston et al., 2020; J. Yang et al., 2010). In the Central Arctic near Svalbard, ICESat-2  
586 indicates the highest values of sublimation (3-4 cm SWE). A secondary maximum ( $> 3$  cm SWE)  
587 occurs in the Barents Sea, where blowing snow is retrieved half as often. This reflects the  
588 sensitivity of sublimation to temperature and humidity, because the marginal seas are generally  
589 warmer than the Central Arctic (Fig. S7). Thus, the reduced occurrence of blowing snow is offset  
590 by higher temperatures and lower humidity, which enhance sublimation.

591

592 The average blowing snow sublimation derived from ICESat-2 over first-year sea ice is 1.47 cm  
593 SWE (SnowModel-LG: 1.66 cm SWE; DY2001: 2.02 cm SWE), compared to 2.06 cm SWE  
594 over multi-year ice (SnowModel-LG: 1.81 cm SWE; DY2001: 2.21 cm SWE). While multi-year  
595 ice constitutes only 25% of our study area, it accounts for 30-35% of the seasonal blowing snow  
596 sublimation. This disproportionate contribution is consistent with the spatial pattern of blowing  
597 snow shown above (Fig. 3), where the region of elevated winds and occurrence is split by the  
598 transition between first- and multi-year ice.

599

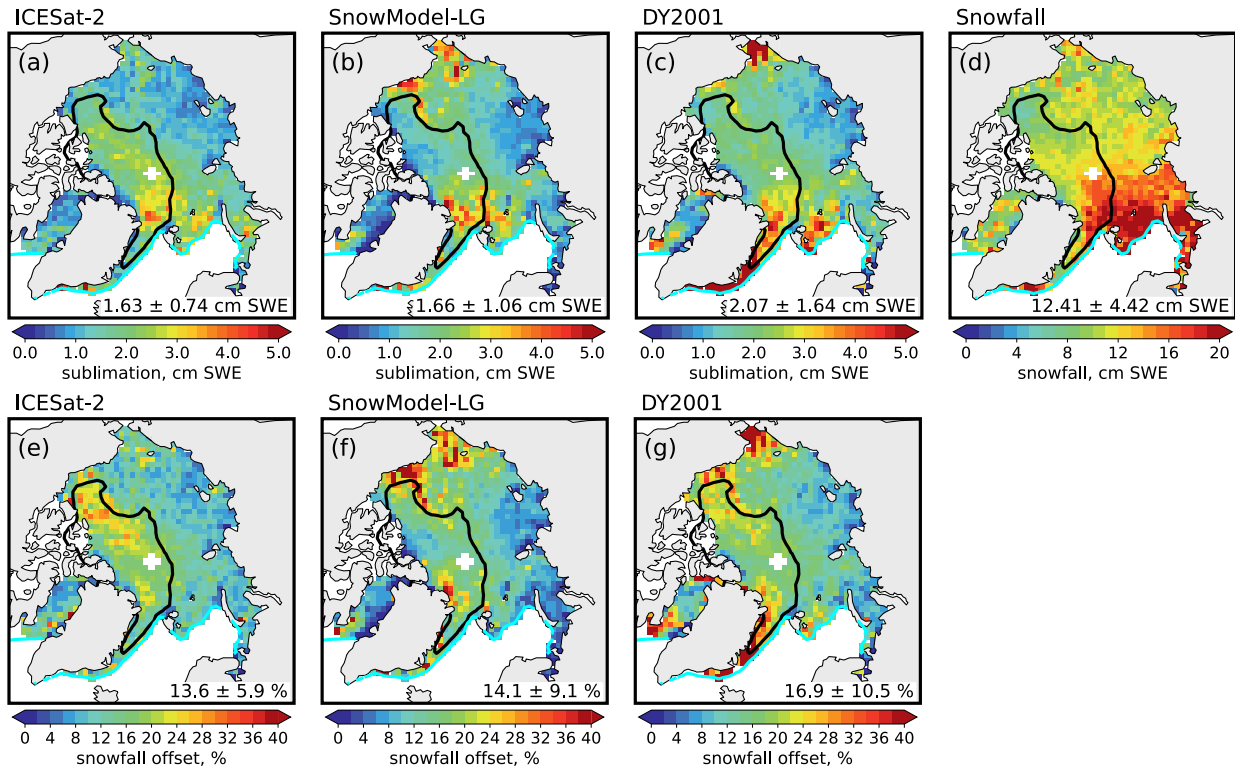
600 We compare blowing snow sublimation to total MERRA-2 snowfall over the cold season (12.41  
601 cm SWE, Fig. 9d). On average, we find that blowing snow removes 13.6% (ICESat-2), 14.1%  
602 (SnowModel-LG), and 16.9% (DY2001) of snowfall. The regional impact, however, varies  
603 strongly (Figs. 9e-g). In the Kara and Barents Seas, where snowfall is highest, sublimation  
604 removes only 5-10% of snowfall. In the Central Arctic losses increase to 18-24%, while in  
605 regions with more moderate snowfall, such as the Beaufort Sea, sublimation losses can exceed  
606 30% (e.g., 2-3 cm SWE of sublimation compared to 8-10 cm SWE of snowfall).

607

608 The fraction of snowfall removed by blowing snow sublimation inferred from ICESat-2 reaches  
609 30% in the Beaufort Sea north of the Canadian Arctic Archipelago (Fig. 9e). SnowModel-LG  
610 and DY2001 show a similar enhanced offset, though their maxima are shifted southwestward  
611 along the coast of Alaska (Fig. 9f,g). The 2018-2023 period was marked by several strong  
612 Beaufort High episodes, such as the 2020-2021 event highlighted in Fig. 5, which are typically  
613 associated with calm, dry conditions. Under such conditions, ICESat-2 retrievals may  
614 occasionally overestimate blowing snow. False positives could arise when low-level ice crystals  
615 (ice clouds or diamond dust) mix with blowing snow, leading the entire ICESat-2 backscatter  
616 signal to misattributed to blowing snow. This effect was most pronounced during winter 2021-

617 2022, when exceptionally warm ( $T > -20^{\circ}\text{C}$ ) and dry ( $\text{RH}_{\text{ice}} < 90\%$ ) conditions prevailed north of  
 618 the Canadian Arctic Archipelago (Fig. S8).

619  
 620 The fraction of snowfall removed by blowing snow sublimation, as inferred from ICESat-2, also  
 621 varies by ice type. On average, values over multi-year ice (15-22%) are 1.6 times larger than  
 622 over first-year ice (9-14%). The enhanced offsets reflects both stronger sublimation and overall  
 623 lower snowfall over multi-year ice (11.43 cm SWE) compared to first-year ice (12.64 cm SWE).  
 624

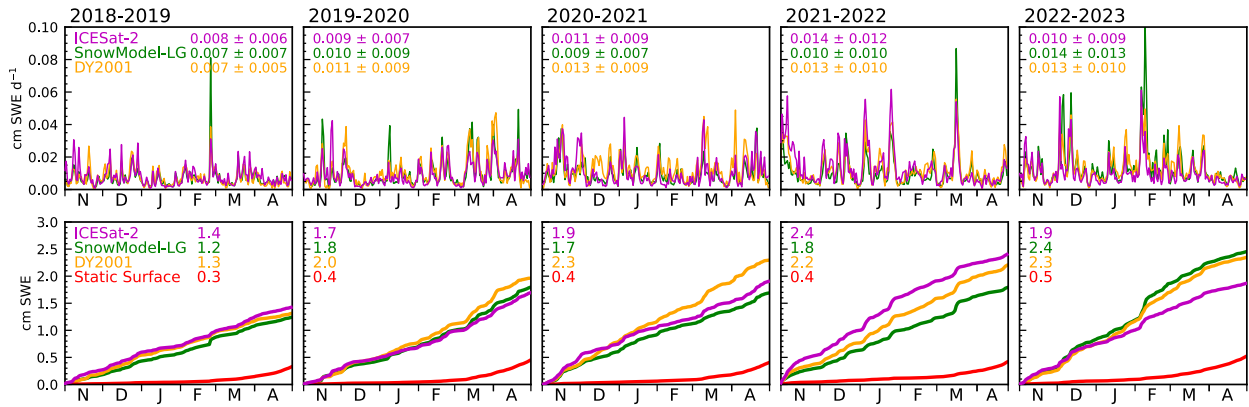


625  
 626 **Figure 9.** Spatial distribution of blowing snow sublimation, total snowfall, and the contribution of blowing snow  
 627 sublimation to snowfall offset over Arctic sea ice during 2018-2023. **(a-c)** Total blowing snow sublimation (cm  
 628 SWE) inferred from (a) ICESat-2, (b) SnowModel-LG, and (c) DY2001. **(d)** Total MERRA-2 snowfall (cm SWE).  
 629 **(e-g)** Percent of snowfall removed by blowing snow sublimation ( $= 100 \times [\text{sublimation} / \text{snowfall}]$ ) from (e) ICESat-  
 630 2, (f) SnowModel-LG, and (g) DY2001. The cyan line marks the 15% sea ice concentration contour and the black  
 631 line delineates regions of first- and multi-year sea ice.

632  
 633 Along Greenland's east coast, DY2001 predicts much higher sublimation fluxes (4-5 cm SWE, >  
 634 70% of snowfall) than either ICESat-2 and SnowModel-LG (2-3 cm SWE, 20-30% of snowfall).  
 635 This discrepancy likely reflects DY2001's simple threshold-based parameterization, which tends  
 636 to overpredict blowing snow at the typical windspeeds in this region (6-8  $\text{m s}^{-1}$ , Fig. 3). Warmer  
 637 and drier conditions in this region (Fig. S7) further amplify the sublimation predicted by  
 638 DY2001.

639  
 640 Daily pan-Arctic time series (Fig. 10) show that blowing snow sublimation is nearly continuous  
 641 throughout the cold season, punctuated by sharp peaks during major storm events. The most  
 642 intense episodes ( $> 0.04 \text{ cm SWE d}^{-1}$  averaged over sea ice) occur only a few times per season  
 643 and correspond to widespread blowing snow detected by ICESat-2 (Fig. S4). These storms

644 contribute disproportionately to the seasonal total, with individual events removing up to 60% of  
 645 daily snowfall (Fig. S9). Between storms, sublimation persists at lower but steady rates (0.01-  
 646 0.02 cm SWE d<sup>-1</sup>) and these background losses accumulate to a substantial share (35-40%) of the  
 647 seasonal total.  
 648



649  
 650 **Figure 10.** Timeseries of blowing snow sublimation across five Arctic cold seasons. **(top row)** Daily blowing snow  
 651 sublimation (cm SWE d<sup>-1</sup>) inferred from ICESat-2 (magenta line) and predicted by SnowModel-LG (green line) and  
 652 DY2001 (orange line). **(bottom row)** Cumulative daily blowing snow sublimation (cm SWE). The red lines in the  
 653 bottom row represent the cumulative static surface (non-blowing snow) sublimation predicted by SnowModel-LG.  
 654

655  
 656 The ICESat-2 inferred sublimation ranges from 1.4 to 2.4 cm SWE across the five cold seasons  
 657 (Fig. 10, bottom row), corresponding to a 11-20% offset of seasonal snowfall. Both snowfall and  
 658 blowing snow sublimation vary by 1-2 cm SWE year to year, but the two do not always covary.  
 659 For example, the 2021-2022 cold season had the lowest snowfall (11.9 cm SWE) yet the highest  
 660 ICESat-2 sublimation (2.4 cm SWE, 20% offset). Conversely, 2018-2019 featured higher  
 661 snowfall (12.9 cm SWE) but relatively low sublimation (1.4 cm SWE, 11% offset). These  
 662 interannual differences highlight that sublimation depends not only on storm frequency and  
 663 strength (which also drive snowfall) but also on atmospheric conditions which regulate blowing  
 664 snow occurrence and sublimation efficiency. SnowModel-LG and DY2001 generally agree with  
 665 the ICESat-2 sublimation, though DY2001 tends to predict slightly higher values.  
 666

667 Blowing snow sublimation exceeds surface sublimation by a factor of 4-5, underscoring the  
 668 dominant role of blowing snow in sublimation-driven snow loss during much of the cold season.  
 669 The cumulative surface sublimation timeseries ( $Q_{ss}$  in Eq. 1) predicted by SnowModel-LG is  
 670 shown in Fig. 10 (red lines, bottom row). Seasonal total surface sublimation averages only 0.3-  
 671 0.5 cm SWE, with nearly all of it occurring from late February through April, when solar  
 672 radiation increases, near-surface air warms, and RH<sub>ice</sub> decreases. These values are lower than the  
 673 1-2 cm SWE reported by Déry and Yau (2002), likely because their annual means included the  
 674 warmer spring and summer months. Consistent with this, SnowModel-LG calculates an Arctic-  
 675 wide annual mean surface sublimation of ~ 1 cm SWE.  
 676

677 ICESat-2 likely underestimates blowing snow sublimation because it cannot observe blowing  
 678 snow beneath optically thick clouds. These conditions are most frequent during winter storms,  
 679 when strong winds can drive intense sublimation. To assess this sampling bias, we examine the  
 680 2018-2023 SnowModel-LG and DY2001 predictions under all conditions (i.e., regardless of

681 whether ICESat-2 detected the surface). The all-conditions maps (Fig. S10) show patterns similar  
682 to Fig. 9 but with magnitudes 16-25% larger. Pan-Arctic blowing snow sublimation totals  
683 increase to 2.1 cm SWE for SnowModel-LG and 2.4 cm SWE for DY2001. Comparing these  
684 values to the seasonal snowfall from Fig. 9 (12.4 cm SWE) yields offsets of 17% for  
685 SnowModel-LG and 19% for DY2001. This comparison suggests that ICESat-2 captures the  
686 spatial pattern and temporal variability of blowing snow sublimation well but underestimates the  
687 total by roughly 20% due to this sampling bias.

688

## 689 **5 Summary and conclusions**

690

691 We presented the first multi-year pan-Arctic estimates of blowing snow derived from ICESat-2  
692 satellite observations, extending our earlier single-year analysis (Robinson et al., 2025) to five  
693 cold seasons (November through April, 2018-2023). ICESat-2 retrievals allowed us to  
694 characterize blowing snow occurrence and properties (geometric and optical depths), and, when  
695 combined with assumptions about particle sizes and meteorology from reanalysis, to infer  
696 blowing snow sublimation and evaluate its contribution to the Arctic snow-on-sea ice budget.

697

698 Over the five seasons analyzed, ICESat-2 retrievals indicate a mean pan-Arctic blowing snow  
699 occurrence of 19%, with maxima exceeding 30% in the Central Arctic and Atlantic sector,  
700 regions frequently impacted by storms arriving from lower latitudes. Retrieved blowing snow  
701 geometric and optical depths also maximize in these regions. Interannual variability of blowing  
702 snow occurrence is substantial and is driven by the Arctic Oscillation (AO). We find that positive  
703 AO periods have lower SLP and higher winds, and ~ 50% more blowing snow than negative AO  
704 periods. In the Central Arctic, blowing snow occurrence during the positive AO phase was more  
705 than twice that of the negative phase, a pattern consistent across all five seasons.

706

707 ICESat-2 observations confirm that windspeed is the primary driver of blowing snow  
708 occurrence, with temperature acting as a secondary modulating factor. Blowing snow occurrence  
709 increases with windspeed across all temperatures, exceeding 80% at 12 m s<sup>-1</sup>. The physics-based  
710 threshold windspeed in SnowModel-LG (4-5 m s<sup>-1</sup>) is 2-3 m s<sup>-1</sup> lower than in DY2001 (~ 7 m s<sup>-1</sup>)  
711 and aligns more closely with the windspeeds at which ICESat-2 reliably detects blowing snow.  
712 Both ICESat-2 and SnowModel-LG suggest blowing snow occurrence frequencies of 10-40% at  
713 windspeeds 4-7 m s<sup>-1</sup>, where DY2001 predicts no blowing snow. Windspeed also strongly  
714 controls blowing snow height and optical depth: blowing snow heights increase from 30 m at 4  
715 m s<sup>-1</sup> to almost 200 m at 15 m s<sup>-1</sup>, while optical depths rise from 0.02 to 0.26 over the same  
716 range, driven by enhanced backscatter over deeper heights.

717

718 Maximum mass transport fluxes peak where blowing snow is most frequent, with seasonal  
719 means of 74 Mg m<sup>-1</sup> for ICESat-2 and 21 Mg m<sup>-1</sup> for SnowModel-LG. This factor of three  
720 difference reflects SnowModel-LG's confinement of blowing snow to the lowest few meters,  
721 where winds are weaker, while ICESat-2 detects layers extending to several hundreds of meters,  
722 where stronger winds drive greater transport. Yet, pan-Arctic burdens agree within ~20% (0.17 g  
723 m<sup>-2</sup> for ICESat-2 vs. 0.14 g m<sup>-2</sup> for SnowModel-LG), underscoring that while the vertical extent  
724 is different, the overall mass is consistent. Despite high transport, divergence in ICESat-2  
725 inferred mass flux contributes minimally to the snow budget (maximum of 1 mm SWE).

726

727 We find that blowing snow sublimation plays an important role in the Arctic snow-on-sea-ice  
728 budget, reaching up to 5 cm SWE in the Central Arctic, and averaging 1.63-2.07 cm SWE over  
729 all sea ice. This is equivalent to a 13.6-16.9% removal of seasonal snowfall on average, with as  
730 much as 30% removal in some regions such as the Beaufort Sea. Blowing snow sublimation  
731 derived from ICESat-2 is consistently larger over multi-year sea ice (2.06 cm SWE) than first-  
732 year sea ice (1.47 cm SWE), corresponding to a 1.6 times larger fraction of snowfall removed  
733 (15-22% vs. 9-14%). The pan-Arctic ICESat-2 inferred blowing snow sublimation ranged from  
734 1.4 to 2.4 cm SWE (11-20% snowfall offset) across the five cold seasons, with similar estimates  
735 from SnowModel-LG (1.2-2.4 cm SWE) and DY2001 (1.3-2.3 cm SWE). SnowModel-LG and  
736 DY2001 predictions under all conditions (i.e., including those without ICESat-2 observations  
737 due to sampling or clouds) suggest pan-Arctic blowing snow sublimation could be ~20% larger  
738 (2.1-2.4 cm SWE) than was found using ICESat-2, resulting in a larger snowfall removal of 17-  
739 19%. SnowModel-LG indicates that sublimation from blowing snow is up to a factor of five  
740 larger than surface sublimation, which offsets only an additional 2-4% of snowfall.

741  
742 Our analysis is limited by a number of factors, including the sampling pattern of ICESat-2.  
743 While the high resolution of atmospheric backscatter allows unprecedented detail into blowing  
744 snow, the narrow spatial sampling requires temporal and spatial averaging, such as binning the  
745 ICESat-2 profiles to a 100 km grid, to generate meaningful statistics. This approach improves  
746 coverage but smooths fine-scale variability and may underrepresent short-lived or localized  
747 blowing snow events. Moreover, the blowing snow algorithm cannot detect blowing snow layers  
748 thinner than 20-30 m. Such thin drifting and blowing snow layers are often predicted by  
749 SnowModel-LG and DY2001. Nevertheless, these discrepancies in vertical resolution and  
750 sampling appear to have a minimal net effect on the overall estimates of blowing snow fluxes,  
751 which are similar for all three methods. Our transport and sublimation flux estimates rely on  
752 reanalysis meteorology, which has been shown to have biases, particularly at high latitudes (e.g.,  
753 Jonassen et al., 2019; Marshall et al., 2018), and currently does not include feedbacks from  
754 blowing snow on the temperature and moisture fields. Such feedbacks would tend to suppress  
755 sublimation by increasing humidity and cooling the near-surface atmosphere, potentially leading  
756 to overestimation of sublimation in our analysis. However, work done on Antarctic blowing  
757 snow processes indicates that the entrainment of warmer and drier air present above the blowing  
758 snow and surface temperature inversion can reduce or even eliminate this sublimation-humidity  
759 feedback (Palm et al., 2018). Incorporating these processes into coupled models would improve  
760 the realism of both meteorological forcing and snow-atmosphere interactions.

761  
762 Beyond its role in the snow-on-sea-ice budget, blowing snow sublimation also acts as a  
763 significant source of moisture and a sink of heat for the atmosphere. The fate of this moisture  
764 remains poorly constrained and warrants further study. Blowing snow sublimation over sea ice is  
765 also a recognized source of sea salt aerosols (e.g., Frey et al., 2020; Gong et al., 2023; J. Huang  
766 & Jaeglé, 2017; Ranjithkumar et al., 2025). Taken together, these points highlight that blowing  
767 snow has the potential to impact a range of polar processes including boundary layer structure,  
768 cloud formation and lifetime, atmospheric chemistry, and the surface energy balance. Recent  
769 modeling efforts are beginning to account for these processes (e.g., Hofer et al., 2021; Luo et al.,  
770 2021), offering new opportunities to improve predictions of Arctic composition, weather, and  
771 climate. Such advancements will require robust observational constraints to ensure realism and  
772 guide a process-based understanding of the coupled Arctic system. By capturing the vertical and

773 horizontal structure of blowing snow at unprecedented scales, our study demonstrates that  
774 spaceborne lidar is a key tool for bridging the gap between observations and models, and for  
775 advancing our understanding of the rapidly changing Arctic environment.

776  
777  
778  
779  
780

#### 781 **Code and data availability**

782  
783 The ICESat-2 ATL09 data used in this study can be accessed through the NASA NSIDC Distributed Active Archive  
784 Center (<https://doi.org/10.5067/ATLAS/ATL09.006>). The code and data required to reproduce the figures in this  
785 study are available at: <https://doi.org/10.5281/zenodo.18119606>.

#### 786 787 **Author contributions**

788  
789 JR and LJ designed the study. SPP aided in ICESat-2 software development and visualization. GEL developed the  
790 SnowModel-LG code. JR and LJ performed formal analysis. JR prepared the manuscript with contributions from all  
791 co-authors.

#### 792 793 **Competing interests**

794  
795 The authors declare that they have no conflict of interest.

#### 796 797 **Acknowledgments**

798  
799 The authors express gratitude to the ICESat-2 engineering and science teams for their ongoing efforts to maintain  
800 the ATLAS instrument and generate the ICESat-2 atmospheric data products.

#### 801 802 **References**

- 803  
804 Ballinger, T. J., Walsh, J. E., Bhatt, U. S., Bieniek, P. A., Tschudi, M. A., Brettschneider, B., Eicken, H., Mahoney,  
805 A. R., Richter-Menge, J., & Shapiro, L. H.: Unusual West Arctic Storm Activity During Winter 2020: Another  
806 Collapse of the Beaufort High? *Geophysical Research Letters*, 48(13). <https://doi.org/10.1029/2021gl092518>, 2021.  
807 Bintanja, R.: The impact of Arctic warming on increased rainfall. *Scientific Reports*, 8(1), 16001.  
808 <https://doi.org/10.1038/s41598-018-34450-3>, 2018.  
809 Bintanja, R., & Andry, O.: Towards a rain-dominated Arctic. *Nature Climate Change*, 7(4), 263–267.  
810 <https://doi.org/10.1038/nclimate3240>, 2017.  
811 Brodzik, M. J., & Knowles, K. W.: Chapter 5: EASE-grid: A versatile set of equal-area projections and grids. In M.  
812 F. Goodchild (Ed.), *Discrete global grids: A web book* (pp. 98–113). Santa Barbara, CA: National Center for  
813 Geographic Information & Analysis. Retrieved from <https://escholarship.org/uc/item/9492q6sm>, 2002.  
814 Chen, W.-N., Chiang, C.-W., & Nee, J.-B.: Lidar ratio and depolarization ratio for cirrus clouds. *Applied Optics*,  
815 41(30), 6470. <https://doi.org/10.1364/AO.41.006470>, 2002.  
816 Chung, Y.-C., Bélair, S., & Mailhot, J.: Blowing Snow on Arctic Sea Ice: Results from an Improved Sea Ice–Snow–  
817 Blowing Snow Coupled System. *Journal of Hydrometeorology*, 12(4), 678–689.  
818 <https://doi.org/10.1175/2011JHM1293.1>, 2011.  
819 Clancy, R., Bitz, C. M., Blanchard-Wrigglesworth, E., McGraw, M. C., & Cavallo, S. M.: A cyclone-centered  
820 perspective on the drivers of asymmetric patterns in the atmosphere and sea ice during Arctic cyclones. *Journal of*  
821 *Climate*, 1–47. <https://doi.org/10.1175/JCLI-D-21-0093.1>, 2022.  
822 Dai, A.: Temperature and pressure dependence of the rain-snow phase transition over land and ocean. *Geophysical*  
823 *Research Letters*, 35(12). <https://doi.org/10.1029/2008gl033295>, 2008.

824 Déry, S. J., & Tremblay, L.-B.: Modeling the Effects of Wind Redistribution on the Snow Mass Budget of Polar Sea  
825 Ice. *Journal of Physical Oceanography*, 34(1), 258–271. [https://doi.org/10.1175/1520-](https://doi.org/10.1175/1520-0485(2004)034<0258:MTEOWR>2.0.CO;2)  
826 0485(2004)034<0258:MTEOWR>2.0.CO;2, 2004.

827 Déry, S. J., & Yau, M. K.: A Bulk Blowing Snow Model. *Boundary-Layer Meteorology*, 93(2), 237–251.  
828 <https://doi.org/10.1023/A:1002065615856>, 1999.

829 Déry, S. J., & Yau, M. K.: Simulation Of Blowing Snow In The Canadian Arctic Using A Double-Moment Model.  
830 *Boundary-Layer Meteorology*, 99(2), 297–316. <https://doi.org/10.1023/A:1018965008049>, 2001.

831 Déry, S. J., & Yau, M. K.: Large-scale mass balance effects of blowing snow and surface sublimation. *Journal of*  
832 *Geophysical Research: Atmospheres*, 107(D23). <https://doi.org/10.1029/2001JD001251>, 2002.

833 Frey, M. M., Norris, S. J., Brooks, I. M., Anderson, P. S., Nishimura, K., Yang, X., Jones, A. E., Nerentorp  
834 Mastromonaco, M. G., Jones, D. H., & Wolff, E. W.: First direct observation of sea salt aerosol production from  
835 blowing snow above sea ice. *Atmospheric Chemistry and Physics*, 20(4), 2549–2578. [https://doi.org/10.5194/acp-](https://doi.org/10.5194/acp-20-2549-2020)  
836 20-2549-2020, 2020.

837 Gallée, H., Guyomarc’h, G., & Brun, E.: Impact Of Snow Drift On The Antarctic Ice Sheet Surface Mass Balance:  
838 Possible Sensitivity To Snow-Surface Properties. *Boundary-Layer Meteorology*, 99(1), 1–19.  
839 <https://doi.org/10.1023/A:1018776422809>, 2001.

840 Gallée, H., Trouvilliez, A., Agosta, C., Genthon, C., Favier, V., & Naaim-Bouvet, F.: Transport of Snow by the  
841 Wind: A Comparison Between Observations in Adélie Land, Antarctica, and Simulations Made with the Regional  
842 Climate Model MAR. *Boundary-Layer Meteorology*, 146(1), 133–147. <https://doi.org/10.1007/s10546-012-9764-z>,  
843 2013.

844 Gelaro, R., McCarty, W., Suárez, M. J., Todling, R., Molod, A., Takacs, L., Randles, C. A., Darmenov, A.,  
845 Bosilovich, M. G., Reichle, R., Wargan, K., Coy, L., Cullather, R., Draper, C., Akella, S., Buchard, V., Conaty, A.,  
846 da Silva, A. M., Gu, W., ... Zhao, B.: The Modern-Era Retrospective Analysis for Research and Applications,  
847 Version 2 (MERRA-2). *Journal of Climate*, 30(14), 5419–5454. <https://doi.org/10.1175/JCLI-D-16-0758.1>, 2017.

848 Gong, X., Zhang, J., Croft, B., Yang, X., Frey, M. M., Bergner, N., Chang, R. Y.-W., Creamean, J. M., Kuang, C.,  
849 Martin, R. V., Ranjithkumar, A., Sedlacek, A. J., Uin, J., Willmes, S., Zawadowicz, M. A., Pierce, J. R., Shupe, M.  
850 D., Schmale, J., & Wang, J.: Arctic warming by abundant fine sea salt aerosols from blowing snow. *Nature*  
851 *Geoscience*, 16(9), 768–774. <https://doi.org/10.1038/s41561-023-01254-8>, 2023.

852 Herzfeld, U., Hayes, A., Palm, S., Hancock, D., Vaughan, M., & Barbieri, K.: Detection and Height Measurement of  
853 Tenuous Clouds and Blowing Snow in ICESat-2 ATLAS Data. *Geophysical Research Letters*, 48(17),  
854 e2021GL093473. <https://doi.org/10.1029/2021GL093473>, 2021.

855 Hofer, S., Amory, C., Kittel, C., Carlsen, T., Le Toumelin, L., & Storelvmo, T.: The Contribution of Drifting Snow  
856 to Cloud Properties and the Atmospheric Radiative Budget Over Antarctica. *Geophysical Research Letters*, 48(22).  
857 <https://doi.org/10.1029/2021gl094967>, 2021.

858 Huang, J., & Jaeglé, L.: Wintertime enhancements of sea salt aerosol in polar regions consistent with a sea ice  
859 source from blowing snow. *Atmospheric Chemistry and Physics*, 17(5), 3699–3712. [https://doi.org/10.5194/acp-17-](https://doi.org/10.5194/acp-17-3699-2017)  
860 3699-2017, 2017.

861 Huang, J., Jaeglé, L., Chen, Q., Alexander, B., Sherwen, T., Evans, M. J., Theys, N., & Choi, S.: Evaluating the  
862 impact of blowing-snow sea salt aerosol on springtime BrO and O<sub>3</sub> in the Arctic. *Atmospheric Chemistry and*  
863 *Physics*, 20(12), 7335–7358. <https://doi.org/10.5194/acp-20-7335-2020>, 2020.

864 Huang, N., Bao, J., Yu, H., and Li, G.: Snow particle fragmentation enhances snow sublimation, *Atmospheric*  
865 *Chemistry and Physics*, 25, 12535–12548, <https://doi.org/10.5194/acp-25-12535-2025>, 2025.

866 Intrieri, J. M., & Shupe, M. D.: Characteristics and Radiative Effects of Diamond Dust over the Western Arctic  
867 Ocean Region. *Journal of Climate*, 17(15), 2953–2960. [https://doi.org/10.1175/1520-](https://doi.org/10.1175/1520-0442(2004)017<2953:CAREOD>2.0.CO;2)  
868 0442(2004)017<2953:CAREOD>2.0.CO;2, 2004.

869 Jonassen, M. O., Välisuo, I., Vihma, T., Uotila, P., Makshtas, A. P., & Launiainen, J.: Assessment of Atmospheric  
870 Reanalyses With Independent Observations in the Weddell Sea, the Antarctic. *Journal of Geophysical Research:*  
871 *Atmospheres*, 124(23), 12468–12484. <https://doi.org/10.1029/2019jd030897>, 2019.

872 Josset, D., Pelon, J., Garnier, A., Hu, Y., Vaughan, M., Zhai, P., Kuehn, R., & Lucker, P.: Cirrus optical depth and  
873 lidar ratio retrieval from combined CALIPSO-CloudSat observations using ocean surface echo. *Journal of*  
874 *Geophysical Research: Atmospheres*, 117(D5), 2011JD016959. <https://doi.org/10.1029/2011JD016959>, 2012.

875 Kenigson, J. S., & Timmermans, M.-L.: Arctic Cyclone Activity and the Beaufort High. *Journal of Climate*, 34(10),  
876 4119–4127. <https://doi.org/10.1175/jcli-d-20-0771.1>, 2021.

877 King, J. C., Anderson, P. S., Vaughan, D. G., Mann, G. W., Mobbs, S. D., & Vosper, S. B.: Wind-borne  
878 redistribution of snow across an Antarctic ice rise. *Journal of Geophysical Research: Atmospheres*, 109(D11),  
879 2003JD004361. <https://doi.org/10.1029/2003JD004361>, 2004.

880 Krnavek, L., Simpson, W. R., Carlson, D., Domine, F., Douglas, T. A., & Sturm, M.: The chemical composition of  
881 surface snow in the Arctic: Examining marine, terrestrial, and atmospheric influences. *Atmospheric Environment*,  
882 50, 349–359. <https://doi.org/10.1016/j.atmosenv.2011.11.033>, 2012.

883 Kwok, R., & Untersteiner, N.: The thinning of Arctic sea ice. *Physics Today*, 64(4), 36–41.  
884 <https://doi.org/10.1063/1.3580491>, 2011.

885 Lecomte, O., Fichet, T., Flocco, D., Schroeder, D., & Vancoppenolle, M.: Interactions between wind-blown snow  
886 redistribution and melt ponds in a coupled ocean–sea ice model. *Ocean Modelling*, 87, 67–80.  
887 <https://doi.org/10.1016/j.ocemod.2014.12.003>, 2015.

888 Lenaerts, J. T. M., Van Den Broeke, M. R., Déry, S. J., König-Langlo, G., Ettema, J., & Munneke, P. K.: Modelling  
889 snowdrift sublimation on an Antarctic ice shelf. *The Cryosphere*, 4(2), 179–190. [https://doi.org/10.5194/tc-4-179-](https://doi.org/10.5194/tc-4-179-2010)  
890 2010, 2010.

891 Lenaerts, J. T. M., Van Den Broeke, M. R., Van Angelen, J. H., Van Meijgaard, E., & Déry, S. J.: Drifting snow  
892 climate of the Greenland ice sheet: A study with a regional climate model. *The Cryosphere*, 6(4), 891–899.  
893 <https://doi.org/10.5194/tc-6-891-2012>, 2012.

894 Lesins, G., Bourdages, L., Duck, T. J., Drummond, J. R., Eloranta, E. W., & Walden, V. P.: Large surface radiative  
895 forcing from topographic blowing snow residuals measured in the High Arctic at Eureka. *Atmospheric Chemistry*  
896 *and Physics*, 9(6), 1847–1862. <https://doi.org/10.5194/acp-9-1847-2009>, 2009.

897 Li, L., & Pomeroy, J. W. (1997a). Estimates of Threshold Wind Speeds for Snow Transport Using Meteorological  
898 Data. *Journal of Applied Meteorology*, 36(3), 205–213. [https://doi.org/10.1175/1520-](https://doi.org/10.1175/1520-0450(1997)036<0205:EOTWSF>2.0.CO;2)  
899 0450(1997)036<0205:EOTWSF>2.0.CO;2

900 Li, L., & Pomeroy, J. W. (1997b). Probability of occurrence of blowing snow. *Journal of Geophysical Research:*  
901 *Atmospheres*, 102(D18), 21955–21964. <https://doi.org/10.1029/97JD01522>

902 Li, Q., Luo, Y., Yang, X., Zilker, B., Richter, A., Dou, K., Zhou, H., Zhan, K., Si, F., and Liu, W.: Tropospheric  
903 bromine monoxide in Ny-Ålesund: source analysis and impacts on atmospheric chemistry, *EGU*sphere [preprint],  
904 <https://doi.org/10.5194/egusphere-2025-4601>, 2025.

905 Liston, G. E., & Elder, K.: A Meteorological Distribution System for High-Resolution Terrestrial Modeling  
906 (MicroMet). *Journal of Hydrometeorology*, 7(2), 217–234. <https://doi.org/10.1175/jhm486.1>, 2006.

907 Liston, G. E., Haehnel, R. B., Sturm, M., Hiemstra, C. A., Berezovskaya, S., & Tabler, R. D.: Simulating complex  
908 snow distributions in windy environments using SnowTran-3D. *Journal of Glaciology*, 53(181), 241–256.  
909 <https://doi.org/10.3189/172756507782202865>, 2007.

910 Liston, G. E., Itkin, P., Stroeve, J., Tschudi, M., Stewart, J. S., Pedersen, S. H., Reinking, A. K., & Elder, K.: A  
911 Lagrangian Snow-Evolution System for Sea-Ice Applications (SnowModel-LG): Part I—Model Description. *Journal*  
912 *of Geophysical Research: Oceans*, 125(10). <https://doi.org/10.1029/2019JC015913>, 2020.

913 Liston, G. E., Polashenski, C., Rösel, A., Itkin, P., King, J., Merkouriadi, I., & Haapala, J.: A Distributed Snow-  
914 Evolution Model for Sea-Ice Applications (SnowModel). *Journal of Geophysical Research: Oceans*, 123(5), 3786–  
915 3810. <https://doi.org/10.1002/2017JC013706>, 2018.

916 Liston, G. E., & Sturm, M.: A snow-transport model for complex terrain. *Journal of Glaciology*, 44(148), 498–516.  
917 <https://doi.org/10.3189/S0022143000002021>, 1998.

918 Liston, G. E., & Sturm, M.: The role of winter sublimation in the Arctic moisture budget. *Hydrology Research*,  
919 35(4–5), 325–334. <https://doi.org/10.2166/nh.2004.0024>, 2004.

920 Luo, L., Zhang, J., Hock, R., & Yao, Y.: Case Study of Blowing Snow Impacts on the Antarctic Peninsula Lower  
921 Atmosphere and Surface Simulated With a Snow/Ice Enhanced WRF Model. *Journal of Geophysical Research:*  
922 *Atmospheres*, 126(2). <https://doi.org/10.1029/2020jd033936>, 2021.

923 Mann, G. W., Anderson, P. S., & Mobbs, S. D.: Profile measurements of blowing snow at Halley, Antarctica.  
924 *Journal of Geophysical Research: Atmospheres*, 105(D19), 24491–24508. <https://doi.org/10.1029/2000JD900247>,  
925 2000.

926 Markus, T., Neumann, T., Martino, A., Abdalati, W., Brunt, K., Csatho, B., Farrell, S., Fricker, H., Gardner, A.,  
927 Harding, D., Jasinski, M., Kwok, R., Magruder, L., Lubin, D., Luthcke, S., Morison, J., Nelson, R.,  
928 Neuenschwander, A., Palm, S., ... Zwally, J.: The Ice, Cloud, and land Elevation Satellite-2 (ICESat-2): Science  
929 requirements, concept, and implementation. *Remote Sensing of Environment*, 190, 260–273.  
930 <https://doi.org/10.1016/j.rse.2016.12.029>, 2017.

931 Marshall, G. J., Kivinen, S., Jylhä, K., Vignols, R. M., & Rees, W. G.: The accuracy of climate variability and trends  
932 across Arctic Fennoscandia in four reanalyses. *International Journal of Climatology*, 38(10), 3878–3895.  
933 <https://doi.org/10.1002/joc.5541>, 2018.

934 McCrystall, M. R., Stroeve, J., Serreze, M., Forbes, B. C., & Screen, J. A.: New climate models reveal faster and  
935 larger increases in Arctic precipitation than previously projected. *Nature Communications*, 12(1), 6765.  
936 <https://doi.org/10.1038/s41467-021-27031-y>, 2021.

937 Merkouriadi, I., Cheng, B., Graham, R. M., Rösel, A., & Granskog, M. A.: Critical Role of Snow on Sea Ice Growth  
938 in the Atlantic Sector of the Arctic Ocean. *Geophysical Research Letters*, 44(20).  
939 <https://doi.org/10.1002/2017gl075494>, 2017.

940 Merkouriadi, I., Gallet, J., Graham, R. M., Liston, G. E., Polashenski, C., Rösel, A., & Gerland, S.: Winter snow  
941 conditions on Arctic sea ice north of Svalbard during the Norwegian young sea ICE (N-ICE2015) expedition.  
942 *Journal of Geophysical Research: Atmospheres*, 122(20). <https://doi.org/10.1002/2017jd026753>, 2017.

943 Neumann, T. A., Martino, A. J., Markus, T., Bae, S., Bock, M. R., Brenner, A. C., Brunt, K. M., Cavanaugh, J.,  
944 Fernandes, S. T., Hancock, D. W., Harbeck, K., Lee, J., Kurtz, N. T., Luers, P. J., Luthcke, S. B., Magruder, L.,  
945 Pennington, T. A., Ramos-Izquierdo, L., Rebold, T., ... Thomas, T. C.: The Ice, Cloud, and Land Elevation Satellite  
946 – 2 mission: A global geolocated photon product derived from the Advanced Topographic Laser Altimeter System.  
947 *Remote Sensing of Environment*, 233, 111325. <https://doi.org/10.1016/j.rse.2019.111325>, 2019.

948 Nishimura, K., & Nemoto, M.: Blowing snow at Mizuho station, Antarctica. *Philosophical Transactions of the*  
949 *Royal Society A: Mathematical, Physical and Engineering Sciences*, 363(1832), 1647–1662.  
950 <https://doi.org/10.1098/rsta.2005.1599>, 2005.

951 Palm, S. P., Kayetha, V., & Yang, Y.: Toward a Satellite-Derived Climatology of Blowing Snow Over Antarctica.  
952 *Journal of Geophysical Research: Atmospheres*, 123(18). <https://doi.org/10.1029/2018JD028632>, 2018.

953 Palm, S. P., Kayetha, V., Yang, Y., & Pauly, R.: Blowing snow sublimation and transport over Antarctica from 11  
954 years of CALIPSO observations. *The Cryosphere*, 11(6), 2555–2569. <https://doi.org/10.5194/tc-11-2555-2017>,  
955 2017.

956 Palm, S. P., Yang, Y., Herzfeld, U. C., Hancock, D., Hayes, A., Barbieri, J., Wimert, & the ICESat-2 Science Team.:  
957 ATLAS/ICESat-2 L3A Calibrated Backscatter Profiles and Atmospheric Layer Characteristics, Version 6 [Dataset].  
958 NASA National Snow and Ice Data Center Distributed Active Archive Center.  
959 <https://doi.org/10.5067/ATLAS/ATL09.006>, 2023.

960 Palm, S. P., Yang, Y., Herzfeld, U., Hancock, D., Hayes, A., Selmer, P., Hart, W., & Hlavka, D.: ICESat-2  
961 Atmospheric Channel Description, Data Processing and First Results. *Earth and Space Science*, 8(8),  
962 e2020EA001470. <https://doi.org/10.1029/2020EA001470>, 2021.

963 Palm, S. P., Yang, Y., Kayetha, V., & Nicolas, J. P.: Insight into the Thermodynamic Structure of Blowing-Snow  
964 Layers in Antarctica from Dropsonde and CALIPSO Measurements. *Journal of Applied Meteorology and*  
965 *Climatology*, 57(12), 2733–2748. <https://doi.org/10.1175/JAMC-D-18-0082.1>, 2018.

966 Palm, S. P., Yang, Y., Spinhirne, J. D., & Marshak, A.: Satellite remote sensing of blowing snow properties over  
967 Antarctica. *Journal of Geophysical Research*, 116(D16), D16123. <https://doi.org/10.1029/2011JD015828>, 2011.

968 Palm, S. P., Yang, Y., Hertzfeld, U., & Hancock, D.: Ice, Cloud, and Land Elevation Satellite (ICESat-2) Project  
969 Algorithm Theoretical Basis Document for the Atmosphere, Part I: Level 2 and 3 Data Products, version 6.  
970 <https://doi.org/10.5067/H975R4YYVIT6>, 2022.

971 Pomeroy, J. W., Marsh, P., & Gray, D. M.: Application of a distributed blowing snow model to the Arctic.  
972 *Hydrological Processes*, 11(11), 1451–1464. [https://doi.org/10.1002/\(SICI\)1099-1085\(199709\)11:11<1451::AID-  
973 HYP449>3.0.CO;2-Q](https://doi.org/10.1002/(SICI)1099-1085(199709)11:11<1451::AID-HYP449>3.0.CO;2-Q), 1997.

974 Ranjithkumar, A., Duncan, E., Yang, X., Partridge, D. G., Lachlan-Cope, T., Gong, X., Nishimura, K., & Frey, M.  
975 M.: Direct observation of Arctic Sea salt aerosol production from blowing snow and modeling over a changing sea  
976 ice environment. *Elem Sci Anth*, 13(1). <https://doi.org/10.1525/elementa.2024.00006>, 2025.

977 Rantanen, M., Karpechko, A. Yu., Lipponen, A., Nordling, K., Hyvärinen, O., Ruosteenoja, K., Vihma, T., &  
978 Laaksonen, A.: The Arctic has warmed nearly four times faster than the globe since 1979. *Communications Earth &  
979 Environment*, 3(1), 168. <https://doi.org/10.1038/s43247-022-00498-3>, 2022.

980 Rhodes, R. H., Yang, X., Wolff, E. W., McConnell, J. R., & Frey, M. M.: Sea ice as a source of sea salt aerosol to  
981 Greenland ice cores: A model-based study. *Atmospheric Chemistry and Physics*, 17(15), 9417–9433.  
982 <https://doi.org/10.5194/acp-17-9417-2017>, 2017.

983 Rinke, A., Cassano, J. J., Cassano, E. N., Jaiser, R., & Handorf, D.: Meteorological conditions during the MOSAiC  
984 expedition. *Elementa: Science of the Anthropocene*, 9(1), 00023. <https://doi.org/10.1525/elementa.2021.00023>,  
985 2021.

986 Robinson, J., Jaeglé, L., Palm, S. P., Shupe, M. D., Liston, G. E., & Frey, M. M.: ICESat-2 observations of blowing  
987 snow over Arctic sea ice during the 2019–2020 MOSAiC expedition. *Journal of Geophysical Research:  
988 Atmospheres*, 130, e2025JD043919. <https://doi.org/10.1029/2025JD043919>, 2025.

989 Schmidt, R. A.: Vertical profiles of wind speed, snow concentration, and humidity in blowing snow. *Boundary-  
990 Layer Meteorology*, 23(2), 223–246. <https://doi.org/10.1007/BF00123299>, 1982.

991 Serreze, M. C., & Barrett, A. P.: Characteristics of the Beaufort Sea High. *Journal of Climate*, 24(1), 159–182.  
992 <https://doi.org/10.1175/2010jcli3636.1>, 2011.

993 Shupe, M. D., Walden, V. P., Eloranta, E., Uttal, T., Campbell, J. R., Starkweather, S. M., & Shiobara, M.: Clouds  
994 at Arctic Atmospheric Observatories. Part I: Occurrence and Macrophysical Properties. *Journal of Applied  
995 Meteorology and Climatology*, 50(3), 626–644. <https://doi.org/10.1175/2010JAMC2467.1>, 2011.

996 Stroeve, J., & Notz, D.: Changing state of Arctic sea ice across all seasons. *Environmental Research Letters*, 13(10),  
997 103001. <https://doi.org/10.1088/1748-9326/aade56>, 2018.

998 Sturm, M., Holmgren, J., & Perovich, D. K.: Winter snow cover on the sea ice of the Arctic Ocean at the Surface  
999 Heat Budget of the Arctic Ocean (SHEBA): Temporal evolution and spatial variability. *Journal of Geophysical  
1000 Research: Oceans*, 107(C10). <https://doi.org/10.1029/2000jc000400>, 2002.

1001 Tschudi, M. A., Meier, W. N., & Stewart, J. S.: An enhancement to sea ice motion and age products at the National  
1002 Snow and Ice Data Center (NSIDC). *The Cryosphere*, 14(5), 1519–1536. <https://doi.org/10.5194/tc-14-1519-2020>,  
1003 2020.

1004 Tschudi, M. & Univ Of CO.: Polar Pathfinder Daily 25 km EASE-Grid Sea Ice Motion Vectors [Dataset]. NASA  
1005 National Snow and Ice Data Center Distributed Active Archive Center. <https://doi.org/10.5067/INAWUWO7QH7B>,  
1006 2019.

1007 Valkonen, E., Cassano, J., & Cassano, E.: Arctic Cyclones and Their Interactions With the Declining Sea Ice: A  
1008 Recent Climatology. *Journal of Geophysical Research: Atmospheres*, 126(12).  
1009 <https://doi.org/10.1029/2020jd034366>, 2021.

1010 Webster, M., Gerland, S., Holland, M., Hunke, E., Kwok, R., Lecomte, O., Massom, R., Perovich, D., & Sturm, M.:  
1011 Snow in the changing sea-ice systems. *Nature Climate Change*, 8(11), 946–953. [https://doi.org/10.1038/s41558-018-  
1012 0286-7](https://doi.org/10.1038/s41558-018-0286-7), 2018.

1013 Winker, D. M., Vaughan, M. A., Omar, A., Hu, Y., Powell, K. A., Liu, Z., Hunt, W. H., & Young, S. A.: Overview  
1014 of the CALIPSO Mission and CALIOP Data Processing Algorithms. *Journal of Atmospheric and Oceanic  
1015 Technology*, 26(11), 2310–2323. <https://doi.org/10.1175/2009JTECHA1281.1>, 2009.

1016 Yang, J., & Yau, M. K.: A New Triple-Moment Blowing Snow Model. *Boundary-Layer Meteorology*, 126(1), 137–  
1017 155. <https://doi.org/10.1007/s10546-007-9215-4>, 2007.

1018 Yang, J., Yau, M. K., Fang, X., & Pomeroy, J. W.: A triple-moment blowing snow-atmospheric model and its  
1019 application in computing the seasonal wintertime snow mass budget. *Hydrology and Earth System Sciences*, 14(6),  
1020 1063–1079. <https://doi.org/10.5194/hess-14-1063-2010>, 2010.

1021 Yang, X., Frey, M. M., Rhodes, R. H., Norris, S. J., Brooks, I. M., Anderson, P. S., Nishimura, K., Jones, A. E., &  
1022 Wolff, E. W.: Sea salt aerosol production via sublimating wind-blown saline snow particles over sea ice:  
1023 Parameterizations and relevant microphysical mechanisms. *Atmospheric Chemistry and Physics*, 19(13), 8407–  
1024 8424. <https://doi.org/10.5194/acp-19-8407-2019>, 2019.

1025 Yang, X., Pyle, J. A., & Cox, R. A.: Sea salt aerosol production and bromine release: Role of snow on sea ice.  
1026 *Geophysical Research Letters*, 35(16), L16815. <https://doi.org/10.1029/2008GL034536>, 2008.

1027 Yang, Y., Palm, S. P., Marshak, A., Wu, D. L., Yu, H., & Fu, Q.: First satellite-detected perturbations of outgoing  
1028 longwave radiation associated with blowing snow events over Antarctica. *Geophysical Research Letters*, 41(2),  
1029 730–735. <https://doi.org/10.1002/2013GL058932>, 2014.

1030 Zhang, D., Vogelmann, A., Kollias, P., Luke, E., Yang, F., Lubin, D., & Wang, Z.: Comparison of Antarctic and  
1031 Arctic Single-Layer Stratiform Mixed-Phase Cloud Properties Using Ground-Based Remote Sensing Measurements.  
1032 *Journal of Geophysical Research: Atmospheres*, 124(17–18), 10186–10204. <https://doi.org/10.1029/2019JD030673>,  
1033 2019.